

Bragg resonance of waves in a two-layer fluid propagating over bottom ripples. Part II. Numerical simulation.

MOHAMMAD-REZA ALAM,
YUMING LIU AND DICK K. P. YUE†

Department of Mechanical Engineering, Center for Ocean Engineering,
Massachusetts Institute of Technology, Cambridge, MA 02139, USA

(Received 29 November 2007 and in revised form 2 December 2008)

We develop a direct numerical method to study the general problem of nonlinear interactions of surface/interfacial waves with variable bottom topography in a two-layer density stratified fluid. We extend a powerful high-order spectral (HOS) method for nonlinear gravity wave dynamics in a homogeneous fluid to the case of a two-layer fluid over non-uniform bottom. The method is capable of capturing the nonlinear interactions among large number of surface/interfacial wave mode and bottom ripple components up to an arbitrary high order. The method preserves exponential convergence with respect to the number of modes of the original HOS and the (approximately) linear effort with respect to mode number and interaction order. The method is validated through systematic convergence tests and comparison to a semi-analytic solution we obtain for an exact nonlinear Stokes waves on a two-layer fluid (in uniform depth). We apply the numerical method to the three classes of generalized Bragg resonances studied in Alam, Liu & Yue (*J. Fluid Mech.*, vol. 624, 2009, p. 225), and compare the perturbation predictions obtained there with the direct simulation results. An important finding is possibly the important effect of even higher-order nonlinear interactions not accounted for in the leading-order perturbation analyses. To illustrate the efficacy of the numerical method to the general problem, we consider a somewhat more complicated case involving two incident waves and three bottom ripple components with wavenumbers that lead to the possibility of multiple Bragg resonances. It is shown that the ensuing multiple (near) resonant interactions result in the generation of multiple new transmitted/reflected waves that fill a broad wavenumber band eventually leading to the loss of order and chaotic motion.

1. Introduction

Our main objective is the general high-order and multiple Bragg resonance interactions of surface/internal waves in a two-layer stratified fluid propagating over a patch of wavy bottom. This is a follow-on work of part I on this subject (Alam, Liu & Yue 2009), which is motivated by the need for a better understanding of the origin of internal waves in lakes and on continental shelves (e.g. Miropol'sky 2001). Alam *et al.* (2009) present a possible mechanism where bottom ripples play a role, and show, among other things, that conditions for two-layer Bragg resonance can be obtained

† Email address for correspondence: yue@mit.edu

which may explain observations of internal waves in shallower stratified waters (e.g. Boegman *et al.* 2003; Cummins *et al.* 2003).

In Alam *et al.* (2009), we develop perturbation analyses for three different classes of Bragg resonances that obtain when interactions up to third order in wave/bottom steepness are considered. At second order, class I Bragg resonance involves two surface/internal waves and one bottom ripple component. At third order, classes II and III Bragg resonance involve quartets of components: two surface/internal and two bottom ripple components, and three surface/internal waves and one bottom ripple component, respectively. Alam *et al.* (2009) enumerate the multiple possible combinations and cases under these resonance classes, elucidate the different mechanisms and obtain predictions of the (initial) growth/evolution of the resonant wave. While perturbation analyses provide the essential framework and understand specific predictions, the general problem of interest involving multiple (resonantly) interacting surface/internal/bottom components up to high (possibly more than third) order becomes quickly intractable analytically, and numerical solutions must be sought. This is the subject of the present paper.

In this paper, we extend a powerful high-order spectral method (HOS), originally developed for nonlinear wave–wave and wave–bottom interactions in a one-layer fluid (Dommermuth & Yue 1987; Liu & Yue 1998), to the case of a two-layer density stratified fluid. HOS is the extension of Zakharov (1968) mode coupling idea in a direct computational approach. This method computationally accounts for nonlinear wave–wave and wave–bottom interactions up to an arbitrary high-order M in the wave (or bottom) steepness, and follows the (time) evolution of a large number of wave modes, say $N = O(10^3)$ per horizontal dimension. By using the fast transform techniques, the computational effort is (approximately) linearly proportional to M and N . For moderately steep waves and bottom ripples, the method achieves an exponential convergence of the solution with respect to M and N . The extension of HOS to a two-layer fluid over non-uniform bottom preserves these computational properties and is extremely efficient and effective (in some sense ideal) for the problem at hand.

The mathematical formulation of the HOS method for a two-layer fluid in the presence of variable bottom topography is described in §2. In §3, we discuss the implementation issues and present a validation of the method by testing the convergence with different numerical parameters (including N and M) using the fully nonlinear Stokes wave solution in a two-layer fluid as the benchmark. In §4, direct numerical simulations are used to investigate nonlinear resonant interactions of surface/internal waves and bottom undulations. In order to relate the present time-domain simulation to the theoretical results in the frequency domain, we develop (in Appendix C) a robust algorithm for the decomposition of Fourier wave components of a nonlinear wave field from the time history of the wave field evolution.

We obtain quantitative comparison between the numerical prediction and perturbation solution and characterize the higher-order effects (not accounted for in the theory). The three classes of Bragg resonance of surface/internal waves over bottom ripples are studied in §§4.1, 4.2 and 4.3, respectively. In each case, the present HOS predictions are validated and compared against the theoretical predictions of Alam *et al.* (2009). The effects of greater steepness and higher-order interactions on the resonances are then quantified and characterized. Finally, in §4.4, we consider a somewhat more complicated problem involving multiple Bragg resonances with a bottom containing two different (sinusoidal) ripple components. We study the long-time evolution over such a bottom of a biharmonic incident surface wave chosen to

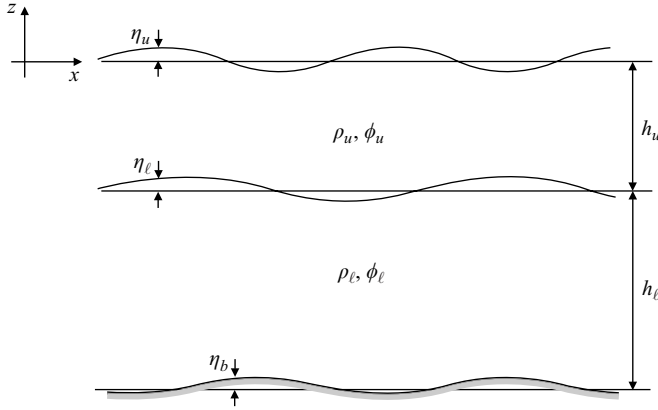


FIGURE 1. Definition sketch.

(initially) satisfy class III Bragg resonance condition. Because of the presence of the additional (resonant) bottom wavenumbers, multiple higher-order resonances ensue as predicted by theory and confirmed numerically. As time increases, these resonant interactions spread the energy in the initial incident waves over a broad range of frequencies, and the wave motion is shown to become chaotic.

2. Mathematical formulation

In this section, we describe the mathematical formulation of a numerical method for the computation of nonlinear interactions of gravity surface and interfacial waves with varying bottom topography. This method is a direct extension of the HOS method for the simulation of nonlinear wave–wave and wave–bottom interactions in a single layer fluid (Dommermuth & Yue 1987; Liu & Yue 1998). The extended method is capable of accounting for nonlinear interactions of broadband wave components on the surface, interface and the bottom up to an arbitrary high order in the wave/bottom steepness.

2.1. Initial boundary-value problem

We consider the motion of a two-layer fluid over a variable bottom topography. A Cartesian coordinate system is defined with the x -axis on the mean free surface and the z -axis positive upward, as shown in figure 1. The upper and lower layers of fluid have, respectively, depths and densities of h_u , ρ_u and h_l , ρ_l (hereafter subscripts u and l are used to denote upper and lower layer quantities, respectively), and the bottom elevation is given by $\eta_b = \eta_b(x)$. In each layer, we assume that the fluid is homogeneous, incompressible, immiscible and inviscid, and the motion irrotational and described by the velocity potential $\phi_u(x, z, t)$ or $\phi_l(x, z, t)$. The equations governing the motion of a two-layer fluid are (ignoring surface tension)

$$\nabla^2 \phi_u = 0, \quad -h_u + \eta_l < z < \eta_u, \quad (2.1a)$$

$$\nabla^2 \phi_l = 0, \quad -h_u - h_l + \eta_b < z < -h_u + \eta_l, \quad (2.1b)$$

$$\eta_{u,t} + \eta_{u,x} \phi_{u,x} - \phi_{u,z} = 0, \quad z = \eta_u, \quad (2.1c)$$

$$\phi_{u,t} + \frac{1}{2} (\phi_{u,x}^2 + \phi_{u,z}^2) + g \eta_u = 0, \quad z = \eta_u, \quad (2.1d)$$

$$\eta_{l,t} + \eta_{l,x} \phi_{l,x} - \phi_{l,z} = 0, \quad z = -h_u + \eta_l, \quad (2.1e)$$

$$\eta_{\ell,t} + \eta_{\ell,x}\phi_{\ell,x} - \phi_{\ell,z} = 0, \quad z = -h_u + \eta_\ell, \quad (2.1f)$$

$$\rho_u \left[\phi_{u,t} + \frac{1}{2}(\phi_{u,x}^2 + \phi_{u,z}^2) + g\eta_\ell \right] - \rho_\ell \left[\phi_{\ell,t} + \frac{1}{2}(\phi_{\ell,x}^2 + \phi_{\ell,z}^2) + g\eta_\ell \right] = 0, \quad z = -h_u + \eta_\ell, \quad (2.1g)$$

$$\eta_{b,x}\phi_{\ell,x} - \phi_{\ell,z} = 0, \quad z = -h_u - h_\ell + \eta_b, \quad (2.1h)$$

where $\eta_u = \eta_u(x, t)$, $\eta_\ell = \eta_\ell(x, t)$, are respectively the free surface and interface wave elevations and g the gravitational acceleration. For an initial-value problem, the conditions are prescribed at initial time ($t=0$) for the surface and interface elevations ($\eta_u(x, 0)$, $\eta_\ell(x, 0)$) and velocity potentials ($\phi_u(x, \eta_u(x, 0), 0)$, $\phi_u(x, -h_u + \eta_\ell(x, 0), 0)$, $\phi_\ell(x, -h_u + \eta_\ell(x, 0), 0)$) are specified. For computation, periodic boundary condition in the horizontal direction is assumed.

2.2. Evolution equations

We define the surface potential ϕ_u^S for the upper layer, and the interface potentials for the upper and lower layers ϕ_u^I and ϕ_ℓ^I as follows:

$$\phi_u^S(x, t) \equiv \phi_u(x, \eta_u(x, t), t) \quad \text{and} \quad \phi_{u/\ell}^I(x, t) \equiv \phi_{u/\ell}(x, -h_u + \eta_\ell(x, t), t). \quad (2.2)$$

In the neighbourhood of the interface, for convenience, we define a new potential $\psi(x, z, t) \equiv \phi_\ell(x, z, t) - \mathcal{R}\phi_u(x, z, t)$, where $\mathcal{R} \equiv \rho_u/\rho_\ell$. We further define ψ^I to be the value of ψ evaluated on the interface

$$\psi^I(x, t) \equiv \phi_\ell^I(x, t) - \mathcal{R}\phi_u^I(x, t). \quad (2.3)$$

In terms of these quantities, we rewrite the kinematic and dynamic boundary conditions on the surface (2.1c) and (2.1d) and interface (2.1e) and (2.1g) in the forms

$$\eta_{u,t} = -\eta_{u,x}\phi_{u,x}^S + (1 + \eta_{u,x}^2)\phi_{u,z}, \quad z = \eta_u, \quad (2.4)$$

$$\phi_{u,t}^S = -g\eta_u - \frac{1}{2}(\phi_{u,x}^S)^2 + \frac{1}{2}(1 + \eta_{u,x}^2)\phi_{u,z}^2, \quad z = \eta_u, \quad (2.5)$$

$$\eta_{\ell,t} = -\eta_{\ell,x}\phi_{\ell,x}^I + (1 + \eta_{\ell,x}^2)\phi_{\ell,z}, \quad z = -h_u + \eta_\ell,$$

$$\psi_{,t}^I = \frac{1}{2}[\mathcal{R}(\phi_{u,x}^I)^2 - (\phi_{\ell,x}^I)^2] \quad (2.6)$$

$$+ \frac{1}{2}(1 + \eta_{\ell,x}^2)(\phi_{\ell,z}^2 - \mathcal{R}\phi_{u,z}^2) - g\eta_\ell(1 - \mathcal{R}), \quad z = -h_u + \eta_\ell. \quad (2.7)$$

In the HOS approach, (2.4)–(2.7) are the evolution equations for η_u , ϕ_u^S , η_ℓ and ψ^I . These depend on the vertical surface velocity $\phi_{u,z}(x, \eta_u, t)$, and the vertical interface velocities $\phi_{u,z}(x, -h_u + \eta_\ell, t)$ and $\phi_{\ell,z}(x, -h_u + \eta_\ell, t)$, which are obtained from the boundary-value problem solution.

2.3. Perturbation expansions

To solve the boundary-value problem, we assume that ϕ_u , ϕ_ℓ , η_u , η_ℓ and η_b and all their derivatives are $O(\epsilon)$, where ϵ is a small quantity that measures the steepness of the free surface, interface and bottom. We expand ϕ_u and ϕ_ℓ in perturbation series up to an arbitrary order M in ϵ

$$\phi_u(x, z, t) = \sum_{m=1}^M \phi_u^{(m)}(x, z, t), \quad \phi_\ell(x, z, t) = \sum_{m=1}^M \phi_\ell^{(m)}(x, z, t), \quad (2.8)$$

where the superscript (m) represents a quantity of $O(\epsilon^m)$.

On the free surface, as in a one-layer fluid, we expand the surface potential $\phi_u^S(x, t)$ in a Taylor series with respect to the mean free surface $z = 0$

$$\phi_u^S(x, t) = \sum_{m=1}^M \phi_u^{(m)}(x, \eta_u, t) = \sum_{m=1}^M \sum_{k=0}^{M-m} \frac{\eta_u^k}{k!} \frac{\partial^k}{\partial z^k} \phi_u^{(m)}(x, z, t) \Big|_{z=0}. \quad (2.9)$$

At each time t , η_u and ϕ_u^S are considered to be known from time integration of (2.4) and (2.5). From (2.9), we now obtain a sequence of Dirichlet boundary conditions on $z = 0$ for $\phi_u^{(m)}$

$$\phi_u^{(m)}(x, 0, t) = f_u^{(m)} \quad (2.10)$$

with

$$f_u^{(1)} = \phi_u^S, \quad (2.11)$$

$$f_u^{(m)} = - \sum_{k=1}^{m-1} \frac{\eta_u^k}{k!} \frac{\partial^k}{\partial z^k} \phi_u^{(m-k)}(x, z, t) \Big|_{z=0}, \quad m = 2, 3, \dots, M. \quad (2.12)$$

Similarly, on the interface, we expand ψ^I in a Taylor series with respect to the mean position of the interface $z = -h_u$

$$\psi^I(x, t) = \sum_{m=1}^M \psi^{(m)}(x, -h_u + \eta_\ell, t) = \sum_{m=1}^M \sum_{k=0}^{M-m} \frac{\eta_\ell^k}{k!} \frac{\partial^k}{\partial z^k} \psi^{(m)}(x, z, t) \Big|_{z=-h_u}. \quad (2.13)$$

As on the free surface, at any time t , η_ℓ and ψ^I are given from integrating (2.6) and (2.7). From (2.13), we again obtain a sequence of Dirichlet boundary conditions on $z = -h_u$ for $\psi^{(m)}$

$$\psi^{(m)}(x, -h_u, t) = f_{\ell 1}^{(m)} \quad (2.14)$$

with

$$f_{\ell 1}^{(1)} = \psi^I, \quad (2.15)$$

$$f_{\ell 1}^{(m)} = - \sum_{k=1}^{m-1} \frac{\eta_\ell^k}{k!} \frac{\partial^k}{\partial z^k} \psi^{(m-k)}(x, z, t) \Big|_{z=-h_u}, \quad m = 2, 3, \dots, M. \quad (2.16)$$

On the interface, there are two kinematic boundary conditions (2.1e) and (2.1f). In addition to (2.6) used as the evolution equation for η_ℓ , the other one can be rewritten as

$$\Phi_{,z}(x, z, t) = \eta_{\ell,x} \Phi_{,x}, \quad z = -h_u + \eta_\ell, \quad (2.17)$$

where $\Phi \equiv \phi_u(x, z, t) - \phi_\ell(x, z, t)$. Note that (2.17) is the difference of (2.1e) and (2.1f). Upon expanding $\Phi(x, z, t)$ on the interface $z = -h_u + \eta_\ell$ in a Taylor series with respect to $z = -h_u$, we have

$$\begin{aligned} \Phi(x, -h_u + \eta_\ell, t) &= \sum_{m=1}^M \Phi^{(m)}(x, -h_u + \eta_\ell, t) \\ &= \sum_{m=1}^M \sum_{k=0}^{M-m} \frac{\eta_\ell^k}{k!} \frac{\partial^k}{\partial z^k} \Phi^{(m)}(x, z, t) \Big|_{z=-h_u}. \end{aligned} \quad (2.18)$$

Substituting (2.18) into (2.17) and collecting terms at each order, we obtain a sequence of Neumann boundary conditions at $z = -h_u$ for $\Phi^{(m)}$

$$\Phi_{,z}^{(m)}(x, -h_u, t) = f_{\ell 2}^{(m)} \quad (2.19)$$

with

$$f_{\ell 2}^{(1)} = 0, \quad (2.20)$$

$$f_{\ell 2}^{(m)} = \sum_{k=1}^{m-1} \frac{\partial}{\partial x} \left[\frac{\eta_{\ell}^k}{k!} \frac{\partial^{(k-1)}}{\partial z^{(k-1)}} \Phi_{.x}^{(m-k)}(x, z, t) \Big|_{z=-h_u} \right], \quad (2.21)$$

for $m = 2, 3, \dots, M$.

On the bottom $z = -h_u - h_{\ell} + \eta_b$, we expand ϕ_{ℓ} in a Taylor series with respect to the mean bottom position $z = -h_u - h_{\ell}$. Upon substituting the expansion into the bottom boundary condition (2.1h), we obtain a sequence of Neumann boundary conditions at $z = -h_u - h_{\ell}$ for $\phi_{\ell}^{(m)}$

$$\phi_{\ell,z}^{(m)}(x, -h_u - h_{\ell}, t) = f_b^{(m)} \quad (2.22)$$

with

$$f_b^{(1)} = 0, \quad (2.23)$$

$$f_b^{(m)} = \sum_{k=1}^{m-1} \frac{\partial}{\partial x} \left[\frac{\eta_b^k}{k!} \frac{\partial^{(k-1)}}{\partial z^{(k-1)}} \phi_{\ell,x}^{(m-k)}(x, z, t) \Big|_{z=-h_u-h_{\ell}} \right], \quad m = 2, 3, \dots, M. \quad (2.24)$$

With these expansions, we now obtain a sequence of linearized boundary-value problems for the perturbed potentials $\phi_u^{(m)}$ and $\phi_{\ell}^{(m)}$, $m = 1, 2, \dots, M$. Specifically, at each order m , $\phi_u^{(m)}$ and $\phi_{\ell}^{(m)}$ satisfy Laplace's equation respectively in the regions $0 \geq z \geq -h_u$ and $-h_u \geq z \geq -h_u - h_{\ell}$ with the boundary conditions: (i) $\phi_u^{(m)}(x, 0, t) = f_u^{(m)}$; (ii) $\psi^{(m)}(x, -h_u, t) = f_{\ell 1}^{(m)}$; (iii) $\Phi_{.z}^{(m)}(x, -h_u, t) = f_{\ell 2}^{(m)}$; (iv) $\phi_{\ell,z}^{(m)}(x, -h_u - h_{\ell}, t) = f_b^{(m)}$; and (v) $\phi_u^{(m)}$ and $\phi_{\ell}^{(m)}$ are periodic in x . These boundary-value problems can be solved sequentially up to an arbitrary order M starting from $m = 1$.

2.4. Spectral solution for $\phi_u^{(m)}$ and $\phi_{\ell}^{(m)}$

We apply the spectral method to solve the boundary-value problems for $\phi_u^{(m)}$ and $\phi_{\ell}^{(m)}$, $m = 1, 2, \dots, M$. At each order m , we construct the solutions of $\phi_u^{(m)}$ and $\phi_{\ell}^{(m)}$ in terms of Fourier basis functions:

$$\phi_u^{(m)}(x, z, t) = \sum_{n=-N}^{N-1} \left\{ A_n^{(m)}(t) \frac{\cosh[k_n(z + h_u)]}{\cosh(k_n h_u)} + B_n^{(m)}(t) \frac{\sinh(k_n z)}{\cosh(k_n h_u)} \right\} e^{ik_n x}, \quad (2.25)$$

$$\phi_{\ell}^{(m)}(x, z, t) = \sum_{n=-N}^{N-1} \left\{ C_n^{(m)}(t) \frac{\cosh[k_n(z + h_u + h_{\ell})]}{\cosh(k_n h_{\ell})} + D_n^{(m)}(t) \frac{\sinh[k_n(z + h_u + h_{\ell})]}{\cosh(k_n h_{\ell})} \right\} e^{ik_n x}, \quad (2.26)$$

where $k_n = 2\pi n/L_x$ with L_x being the length of the computational domain, and $A_n^{(m)}$, $B_n^{(m)}$, $C_n^{(m)}$ and $D_n^{(m)}$ are the complex modal amplitudes. One notes that for sufficiently smooth $\phi_u^{(m)}$ and $\phi_{\ell}^{(m)}$, $A_n^{(m)}$, $B_n^{(m)}$, $C_n^{(m)}$ and $D_n^{(m)}$ decay exponentially in magnitude with $|n|$. Clearly, $\phi_u^{(m)}$ and $\phi_{\ell}^{(m)}$ in (2.25) and (2.26) are harmonic and satisfy the boundary condition (v). The unknown amplitudes $A_n^{(m)}$, $B_n^{(m)}$, $C_n^{(m)}$ and $D_n^{(m)}$ are determined by the imposition of the other four boundary conditions (i), (ii), (iii) and (iv) to $\phi_u^{(m)}$ and $\phi_{\ell}^{(m)}$ in (2.25) and (2.26).

Specifically, $A_n^{(m)}$ is determined from the boundary condition (i), $D_n^{(m)}$ from the boundary condition (iv) and $B_n^{(m)}$ and $C_n^{(m)}$ from the boundary conditions (ii) and (iii).

Upon substitution, we have

$$A_n^{(m)} = \tilde{f}_{un}^{(m)}, \quad (2.27a)$$

$$B_n^{(m)} = [k_n \tilde{f}_{un}^{(m)} \mathcal{R} \sinh k_n h_\ell + \tilde{f}_{bn}^{(m)} \cosh k_n h_u + k_n \tilde{f}_{\ell 1n}^{(m)} \sinh k_n h_\ell \cosh k_n h_u + \tilde{f}_{\ell 2n}^{(m)} \cosh k_n h_u \cosh k_n h_\ell] / \Delta_n, \quad (2.27b)$$

$$C_n^{(m)} = -\cosh k_n h_\ell [-k_n \tilde{f}_{un}^{(m)} \mathcal{R} + \tilde{f}_{bn}^{(m)} (\mathcal{R} \sinh k_n h_u \cosh k_n h_\ell + \sinh k_n h_\ell \cosh k_n h_u) - k_n \tilde{f}_{\ell 1n}^{(m)} \cosh k_n h_u + \tilde{f}_{\ell 2n}^{(m)} \mathcal{R} \sinh k_n h_u] / \Delta_n, \quad (2.27c)$$

$$D_n^{(m)} = \frac{\cosh(k_n h_\ell)}{k_n} \tilde{f}_{bn}^{(m)}, \quad (2.27d)$$

for $n=0, \pm 1, \dots, \pm N$. In (2.27), $\Delta_n \equiv k_n (\cosh k_n h_u \cosh k_n h_\ell + \mathcal{R} \sinh k_n h_u \sinh k_n h_\ell)$, and $\tilde{f}_{un}^{(m)}$, $\tilde{f}_{\ell 1n}^{(m)}$, $\tilde{f}_{\ell 2n}^{(m)}$ and $\tilde{f}_{bn}^{(m)}$ are respectively the n th Fourier modal amplitudes of $f_u^{(m)}$, $f_{\ell 1}^{(m)}$, $f_{\ell 2}^{(m)}$ and $f_b^{(m)}$.

2.5. Evaluation of the interface potentials and surface/interface vertical velocities

Once the boundary-value solution at order m is obtained, the vertical velocities of the fluid on the mean free surface and interface at that order are obtained from (2.25) and (2.26)

$$\phi_{u,z}^{(m)}(x, 0, t) = \sum_{n=-N}^N k_n [A_n^{(m)}(t) \tanh(k_n h_u) + B_n^{(m)}(t)] e^{ik_n x}, \quad (2.28a)$$

$$\phi_{u,z}^{(m)}(x, -h_u, t) = \sum_{n=-N}^N k_n B_n^{(m)}(t) e^{ik_n x}, \quad (2.28b)$$

$$\phi_{\ell,z}^{(m)}(x, -h_u, t) = \sum_{n=-N}^N k_n [C_n^{(m)}(t) \tanh(k_n h_u) + D_n^{(m)}(t)] e^{ik_n x}, \quad (2.28c)$$

for $m = 1, 2, \dots, M$.

After the boundary-value solution is obtained up to the specified order M , the interface potentials and the surface/interface vertical velocities are evaluated by

$$\phi_u^I(x, t) = \sum_{m=1}^M \sum_{k=0}^{M-m} \frac{\eta_u^k}{k!} \frac{\partial^k}{\partial z^k} \phi_u^{(m)}(x, -h_u, t), \quad (2.29a)$$

$$\phi_\ell^I(x, t) = \sum_{m=1}^M \sum_{k=0}^{M-m} \frac{\eta_\ell^k}{k!} \frac{\partial^k}{\partial z^k} \phi_\ell^{(m)}(x, -h_u, t), \quad (2.29b)$$

$$\phi_{u,z}(x, \eta_u, t) = \sum_{m=1}^M \sum_{k=0}^{M-m} \frac{\eta_u^k}{k!} \frac{\partial^{(k+1)}}{\partial z^{(k+1)}} \phi_u^{(m)}(x, 0, t), \quad (2.29c)$$

$$\phi_{u,z}(x, -h_u + \eta_\ell, t) = \sum_{m=1}^M \sum_{k=0}^{M-m} \frac{\eta_\ell^k}{k!} \frac{\partial^{(k+1)}}{\partial z^{(k+1)}} \phi_u^{(m)}(x, -h_u, t), \quad (2.29d)$$

$$\phi_{\ell,z}(x, -h_u + \eta_\ell, t) = \sum_{m=1}^M \sum_{k=0}^{M-m} \frac{\eta_\ell^k}{k!} \frac{\partial^{(k+1)}}{\partial z^{(k+1)}} \phi_\ell^{(m)}(x, -h_u, t), \quad (2.29e)$$

in which the higher z -derivatives of $\phi_{u/\ell}^{(m)}$ are evaluated by converting into x -derivatives using Laplace's equation, e.g. $\phi_{u/\ell,zz}^{(m)} = -\phi_{u/\ell,xx}^{(m)}$, $\phi_{u/\ell,zzz}^{(m)} = -\phi_{u/\ell,zzx}^{(m)}$, etc. The x -derivatives are evaluated easily in the Fourier space.

3. Implementation and validation

3.1. Implementation

The time simulation of nonlinear interactions of surface and interfacial waves with variable bottom topography up to a specified order M consists of two main steps: (a) at each time t , given the surface and interface elevations (η_u, η_ℓ), surface potential (ϕ^S) and a weighted potential combination at the interface ($\psi^I = \phi_\ell^I - \mathcal{R}\phi_u^I$), solve the boundary-value problems for ϕ_u and ϕ_ℓ up to the specified order M and evaluate the surface velocity $\phi_{u,z}(x, \eta_u, t)$ and interface velocities $\phi_{u,z}(x, -h_u + \eta_\ell, t)$ and $\phi_{\ell,z}(x, -h_u + \eta_\ell, t)$; and (b) integrate the evolution equations (2.4)–(2.7), in time to obtain the new values of $\eta_u, \eta_\ell, \phi^S$ and ψ^I at time $t + \Delta t$, where Δt is the time step. The two steps (a) and (b) are repeated starting from initial values.

In the present method, the boundary-value problems for ϕ_u and ϕ_ℓ are solved up to the specified order M by a pseudo-spectral approach. Specifically, all spatial derivatives (of quantities such as $\phi_u^{(m)}$, $\psi^{(m)}$ and $\Phi^{(m)}$) are evaluated in wavenumber space while nonlinear terms and products are calculated in physical space at a discrete set of points $x_j, j = 1, 2, \dots, 2N$ on the mean surface and interface. For Fourier basis functions used, the collocation points $x_j, j = 1, 2, \dots, 2N$, are equally spaced, and fast Fourier transform (FFT) is used to project between the wavenumber and physical domain. For time integration, the fourth-order Runge–Kutta scheme is employed. Overall, the operation count for the solution of the complete problem up to order M is $O(MN \ln N)$ per time step.

We note that in the present implementation, for simplicity, the perturbation expansions of ϕ_u and ϕ_ℓ are constructed assuming the free surface, interface and bottom steepnesses to be of the same order, i.e. $\epsilon_s \sim \epsilon_i \sim \epsilon_b = O(\epsilon)$. The treatment for the potentially interesting case when ϵ_s, ϵ_i and ϵ_b are not of the same order (e.g. Arduin & Magne 2007) is a straightforward extension in the HOS method (see Liu & Yue 1998). In addition, the spectral expansions in (2.25) and (2.26) for $\phi_u^{(m)}$ and $\phi_\ell^{(m)}$ at each order m enable highly efficient transformations between the wavenumber and physical spaces via fast transforms. When different spectral expansions (such as the one satisfying the exact bottom boundary condition in Athanassoulis & Belibassakis 1999) are used, this computation efficiency might not be retained. Furthermore, the present numerical scheme is capable of accounting for interactions of broadband wave components. The extremely high efficiency of the scheme (i.e. approximately linear computational effort with N and M) enables the consideration of large values of N (and M), necessary for the problems involving large wavelength and time-period ratios.

For specific simulations, the bottom ripples are typically placed in a patch centred in the computational domain. The disturbance generated by interactions among surface waves, interfacial waves and bottom ripples propagates towards the side boundaries of the computational domain in time. For a fixed length of the computational domain, the simulation is stopped before these disturbances reach the side boundaries (this is checked by repeating the simulation in a larger computational domain). The simulation time for a given domain can be extended by employing a tapering

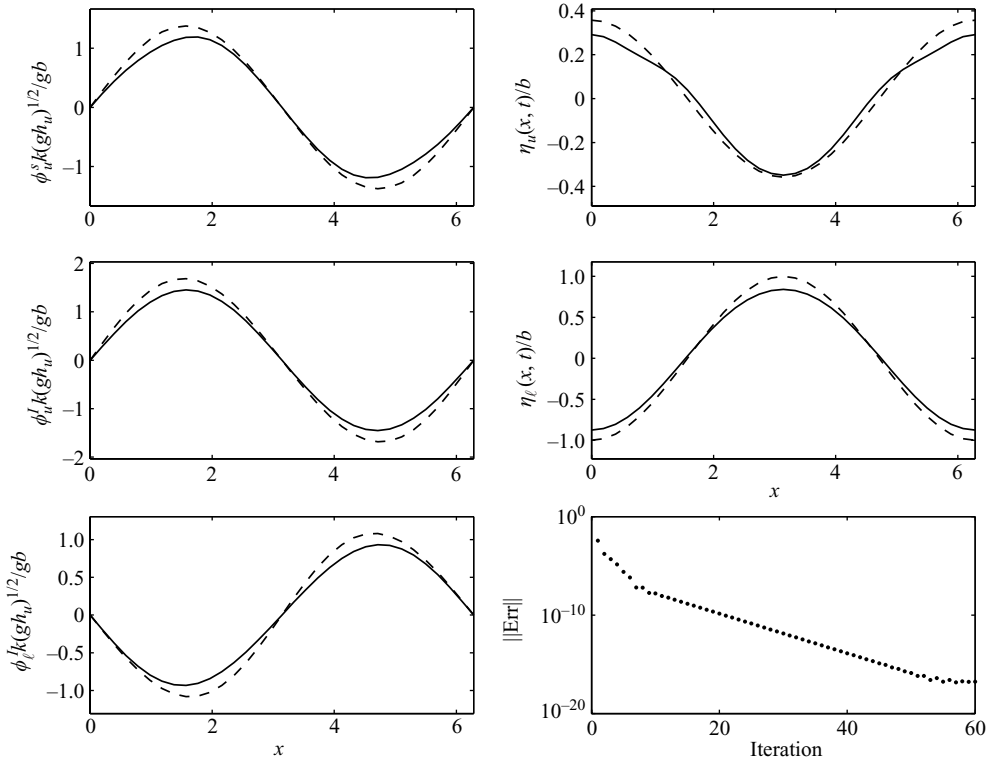


FIGURE 2. Profiles of a steady internal-mode Stokes wave in a two-layer density stratified fluid for the normalized free surface and interface elevations: $\eta_u(x, t)$ and $\eta_\ell(x, t)$; the normalized velocity potentials on the free surface and interface: ϕ_u^S and ϕ_u^I , ϕ_ℓ^I . The plotted curves are the initial guess (---), the solution after 50 iterations (—) and the averaged error as a function of the number of iterations ($\cdot \cdot \cdot$). The physical parameters are $kb = 0.07$, where b is the initial amplitude measured on the interface $h_u/h_\ell = 1/2$, $kh_u = 1$ and $\mathcal{R} = 0.5$.

technique of Dommermuth & Yue (1988) where the solutions are multiplied by a function that tapers smoothly to zero at the two boundaries.

3.2. Convergence tests using a two-layer fluid Stokes wave solution

The HOS method for a one-layer fluid on a rippled bottom has been validated extensively (Liu & Yue 1998). To check the correctness and accuracy of the extension to a two-layer fluid, we use a fully nonlinear solution of a Stokes wave in a two-layer fluid (on a uniform bottom) as a benchmark. The benchmark solution is obtained using Newton's iterative method (see Appendix A). As an example, figure 2 shows the profiles of surface/interface elevations and velocity potentials for a two-layer fluid Stokes wave of the internal mode. The decrease in the error with respect to the number of Newton iterations is also shown. For moderate wave steepness, the error is generally smaller than 10^{-14} after 50 iterations. The benchmark solution used below for the validation of the HOS computations is accurate to 14 decimal places and is hereafter considered to be the 'exact' solution. We first show the convergence of the boundary-value problem solution with respect to the perturbation order M and the number of spectral modes per wavelength N . We specify the boundary conditions on the surface and the interface from the (exact) nonlinear solution of a Stokes wave, and solve for the surface and interface vertical velocities using the HOS approach.

N	$M=1$	$M=2$	$M=3$	$M=4$	$M=6$	$M=8$
4	0.55×10^{-2}	0.13×10^{-2}	0.70×10^{-3}	0.69×10^{-3}	0.69×10^{-3}	0.69×10^{-3}
8	0.90×10^{-3}	0.12×10^{-3}	0.86×10^{-5}	0.21×10^{-5}	0.17×10^{-5}	0.17×10^{-5}
16	0.64×10^{-3}	0.85×10^{-4}	0.60×10^{-5}	0.78×10^{-6}	0.83×10^{-8}	0.67×10^{-9}
32	0.45×10^{-3}	0.60×10^{-4}	0.42×10^{-5}	0.55×10^{-6}	0.55×10^{-8}	0.56×10^{-10}

TABLE 1. Maximum error of the normalized vertical velocity of upper layer fluid at the interface, $\phi_{u,z}(x, -h_u + \eta_\ell, 0)(gh_u)^{1/2}/ga$, for a Stokes wave in a two-layer fluid with $\epsilon=0.1$, $h_\ell/h_u=1$, and $\mathcal{R}=0.5$.

t/T	$T/\Delta t$				
	30	40	50	100	200
1	0.18×10^{-2}	0.72×10^{-3}	0.36×10^{-3}	0.43×10^{-4}	0.53×10^{-5}
10	0.38×10^{-2}	0.14×10^{-2}	0.62×10^{-3}	0.59×10^{-4}	0.65×10^{-5}

TABLE 2. Maximum error of the normalized vertical velocity of the upper layer fluid at the interface, $\phi_{u,z}(x, -h_u + \eta_\ell, t)(gh_u)^{1/2}/ga$, for a Stokes wave in a two-layer fluid with $\epsilon=0.1$, $h_\ell/h_u=1$, and $\mathcal{R}=0.5$ after time integration of $t/T=1, 10$ with different time steps. The HOS parameters are $N=32, M=3$.

The steepness of the nonlinear solution ϵ is defined as the product of the wavenumber and half the crest–trough height. A typical result is given in table 1 for the maximum error in the interface vertical velocity with increasing M and N . For sufficiently large M , the error decays exponentially fast with increasing N . For sufficiently large N , exponential convergence with M is also obtained.

To test the accuracy of the time integration, we use HOS to simulate the nonlinear evolution of the two-layer fluid Stokes wavetrain using the exact solution as initial conditions. Table 2 shows the maximum absolute error in the interface vertical velocity after an evolution of $t/T=1$ and 10 with different time steps. Here T is the fundamental period of the Stokes wave. For these computations, $N=32$ (per wavelength) and $M=3$ are used to ensure that the error in solving the boundary-value problem itself is negligible (see table 1). For the fourth-order Runge–Kutta scheme, the global error decreases as $O((\Delta t/T)^4)$ after a time integration $t/T=O(1)$.

4. Numerical results

The extended HOS method of § 2 is used to perform direct numerical simulations of the nonlinear interactions of surface/interfacial waves with bottom undulations. For further validation, comparisons of the numerical results with theoretical predictions for the second-order two-layer fluid resonant interaction problem with a flat bottom (e.g. Ball 1964; Wen 1995) and experiments of Joyce (1974) are given in Appendix B.

All of the cases identified in Alam *et al.* (2009) for classes I, II and III resonances can and have been investigated by direct HOS simulation (Alam 2008). In addition to further validation of the numerical method (and the theory), of special interest is the effect of higher-order nonlinearities not accounted for in the perturbation theory. It is shown that, in general, high nonlinearity decreases the modulation wavelength/period and amplitude of incident and resonant waves, and down shifts the wavenumber of peak resonance amplitude by altering the dispersion relation. In this section, we focus on the illustrative case studies identified in § 5 of Alam *et al.*

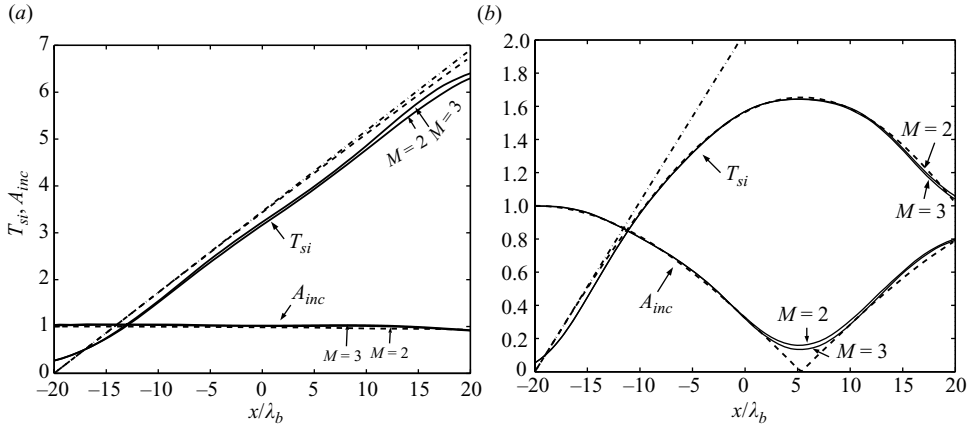


FIGURE 3. Spatial variation of the transmission coefficient of the incident surface-mode wave (A_{inc}) and the resonance generated internal-mode wave (T_{si}) over a patch of bottom ripples under class I Bragg resonance condition. Physical parameters: (a) $\mathcal{R} = 0.96$, $k_s h_u = 0.1$ ($\omega^2 h_u / g = 0.016$), $\epsilon_s = 0.0005$ and (b) $\mathcal{R} = 0.5$, $k_s h_u = 0.35$ ($\omega^2 h_u / g = 0.19$), $\epsilon_s = 0.004$. Common parameters are $h_\ell / h_u = 1$, $\epsilon_b = 0.04$, $M_b = 40$, and computational parameters: $N = 2048$, $M = 2, 3$, $T/\Delta t = 64$ and $T_S/T = 100$. Results plotted are numerical simulation (—) and predictions from regular perturbation (Alam *et al.* 2009, (3.16), - · -) and multiple-scale analyses (Alam *et al.* 2009, (4.6), - - -).

(2009), obtaining direct quantitative comparisons. Finally, as an illustration of the efficacy and application of the numerical method, we use HOS to study the case of long-time interactions involving multiple resonances among the surface, internal and bottom wave components. As time increases, it is shown that the wave motion eventually becomes chaotic.

4.1. Class I Bragg resonance

We apply HOS time simulation to class I Bragg resonant interactions of surface and interfacial waves with a patch of bottom ripples. In addition to cross-validation with the perturbation analysis of Alam *et al.* (2009) for the leading-order effect, we focus also on the effects of higher-order interactions associated with the wave/ripple steepness and the length of the rippled bottom.

When an inter-mode resonance occurs, a new wave-mode is generated. For example, a surface-mode wave may appear on an otherwise flat free surface due to resonant interaction of an internal-mode wave with bottom ripples, and an internal-mode wave can be generated when a surface-mode wave interacts resonantly with bottom ripples.

In the resonance of inter-modes in transmission, the resonant wave travels in the same direction as the incident wave. According to Alam *et al.* (2009), this type of class I Bragg resonance occurs if the bottom wavenumber k_b satisfies the condition $k_b = k_i - k_s$, where k_i and k_s are the wavenumbers of internal and surface-mode waves for any specified frequency ω . Both k_i and k_s are related to ω by the dispersion relation $\mathcal{D}(k_i, \omega) = \mathcal{D}(k_s, \omega) = 0$. There are two cases for this type of resonance: one is with the surface-mode wave as the incident wave and the internal-mode wave as the resonance generated wave ($S_c \xrightarrow{k_b} I_T$) and the other with the internal-mode wave as the incident wave and the surface-mode wave as the generated wave ($I_c \xrightarrow{k_b} S_T$).

For $S_c \xrightarrow{k_b} I_T$, figure 3(a) shows a sample computational result for the variation of the amplitudes of the incident surface-mode wave and the generated internal-mode wave

over a patch of bottom ripples after the steady state of the wave–bottom interaction is reached. Transmission wave amplitudes are extracted from the steady state surface/interface elevations, η_u , η_ℓ (see Appendix C). In this simulation, we use the physical parameters: incident wave steepness $\epsilon_s \equiv k_s a = 0.0005$, depth ratio $h_\ell/h_u = 1$, density ratio $\mathcal{R} = 0.96$, $k_s h_u = 0.1$ ($\omega^2 h_u/g = 0.016$), bottom wavenumber $k_b/k_s = 10$, bottom steepness $\epsilon_b \equiv k_b d = 0.04$ and length of the rippled bottom $M_b = 2L/\lambda_b = 40$; and computational parameters: length of the computational domain $L_x = 2\pi$, total number of spectral modes $N = 2048$, order of nonlinearity $M = 2$ and 3 , time step $T/\Delta t = 64$ and simulation time $T_S/T = 100$, where $T = 2\pi/\omega$ is the period of the incident surface-mode wave (which is equal to the period of the resonance generated wave in class I Bragg resonance). The HOS results are compared to the theoretical predictions of Alam *et al.* (2009) which are second-order regular perturbation theory and multiple-scale analysis. Numerical results agree well with the multiple scales solution and regular perturbation where the latter two are in a good agreement too.

To see a full modulation of the wave amplitudes, the length of the periodic bottom (or the amplitude of incident wave or bottom undulation) has to be greater than that in figure 3(a) ($M_b > O(10^2)$). On the other hand, the amplitude of the resonant transmitted internal wave would become exceedingly large and possibly invalidates the assumptions of the perturbation expansions. Physically, the conditions of M_b (relative to wave and bottom steepnesses) required for a full modulation may also be unlikely to obtain in the ocean (see Ball 1964). To show a case where there is substantial amplitude modulation over a smaller distance and to obtain a clearer picture of such modulation, we consider a stronger stratification of $\mathcal{R} = 0.5$ in figure 3(b) where the HOS results are compared to the theoretical predictions of Alam *et al.* (2009). The direct computational result, which is convergent with M at $M = 2$, compares well with the regular perturbation solution for $x/\lambda_b < O(10)$. Beyond this region, the regular perturbation solution substantially overestimates the growth of the resonant wave. On the other hand, the computational result agrees very well with the solution of the multiple-scale analysis for both incident and resonant waves over the entire patch of bottom ripples. In this case, the amplitude of the resonant (internal mode) wave increases from 0 to $\sim 1.6a$ after a distance of $x \sim 25\lambda_b$, taking almost all of the incident wave energy and then decreases (returning energy to the incident wave).

To show the effect of high-order (in wave and/or bottom steepness) interactions not accounted for in the theory of Alam *et al.* (2009), figure 4 shows a similar case as figure 3(b) but with much greater $\epsilon_s = 0.04$ (all other physical parameters are identical). For HOS, the results for orders $M = 2, 3$ and 4 are given. The numerical results using $M = 3$ have evidently converged and are graphically indistinguishable from those using $M = 4$. The difference between the results for $M = 2$ and those for larger values of M represents the higher-order effects in the wave–bottom interaction not accounted for in the leading order triad class I theory. Clearly, the effect can be appreciable even over relatively short interaction lengths manifest in the reduction in amplitude variations of the incident and the resonant (transmitted) waves, and in the decrease of the (spatial) modulation wavelengths of these interacting wave amplitudes. Note that, because of the higher order nonlinearity, the vanishing of the incident wave amplitude at some interaction distance (as the resonated wave reaches maximum) predicted by the multiple-scale theory analysis does not obtain.

It is of some interest to address the complementary problem of the temporal growth of the resonant wave amplitude over a very long bottom patch. As computation effort increases (linearly) with N , the direct numerical solution of this problem using HOS eventually becomes impractical. If the interactions near the (two) edges of the bottom patch are not of primary concern, the problem can be recast in terms of the time

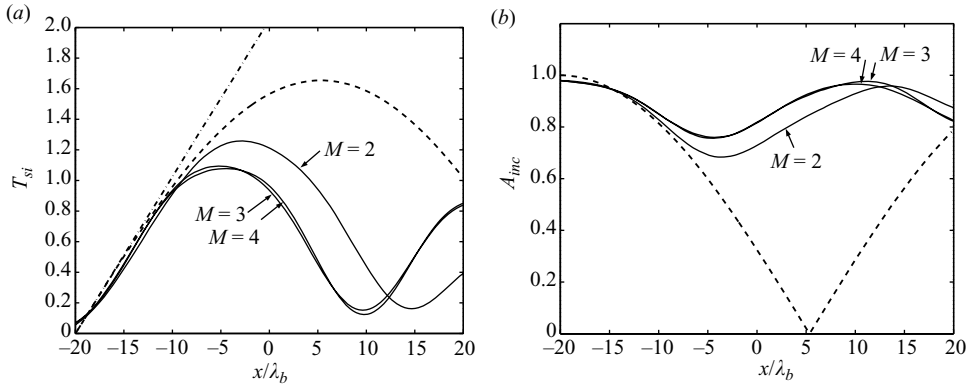


FIGURE 4. Spatial variation of (a) the transmission coefficient of the resonance generated internal-mode wave (T_{si}) and (b) the amplitude of the incident surface-mode wave (A_{inc}), over a patch of bottom ripples under class I Bragg resonance condition. Physical parameters are $h_\ell/h_u = 1$, $\mathcal{R} = 0.5$, $k_s h_u = 0.35$ ($\omega^2 h_u/g = 0.19$), $k_b/k_s = 1.47$, $M_b = 40$, $\epsilon_b = 0.04$, $\epsilon_s = 0.04$ and computational parameters: $N = 2048$, $M = 2, 3$ and 4 , $T/\Delta t = 60$ and $T_S/T = 80$. Results plotted are numerical simulation (—) and predictions from regular perturbation (Alam *et al.* 2009, (3.16), - · -) and multiple-scale analyses (Alam *et al.* 2009, (4.6), - - -).

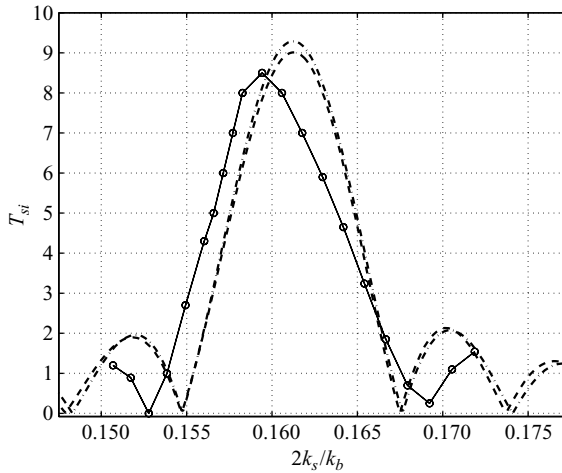


FIGURE 5. Transmission coefficient of the resonant internal-mode wave (T_{si}) due to class I Bragg resonance as a function of wavenumber detuning $2k_s/k_b$. Physical parameters are $h_\ell/h_u = 0.5$, $\mathcal{R} = 0.96$, $k_s h_u = 0.16$ ($\omega^2 h_u/g = 0.04$), $\epsilon_s = 0.005$, $d/h_\ell = 0.1$, $M_b = 20$ and computational parameters: $N = 2048$, $M = 4$, $T/\Delta t = 64$ and $T_S/T = 80$. Results plotted are numerical simulation (—) and predictions from regular perturbation (Alam *et al.* 2009, (3.11), - · -) and multiple-scale analyses (Alam *et al.* 2009, (4.6) and (4.8), - - -).

evolution of waves travelling over a periodic bottom ripple domain (see Alam *et al.* 2009, (B9)). A further discussion and sample simulation results for two cases with $\mathcal{R} = 0.96$ exhibiting full amplitude modulations are given in Appendix D.

As in a one-layer fluid, the nonlinear interactions among the surface and interfacial waves and bottom ripples also change the dispersion relation, and the nonlinear Bragg resonance condition for the interacting wavenumbers is shifted from that given by the linearized dispersion relation. To illustrate this, figure 5 plots the reflection coefficient of the generated wave in the neighbourhood of the class I resonance

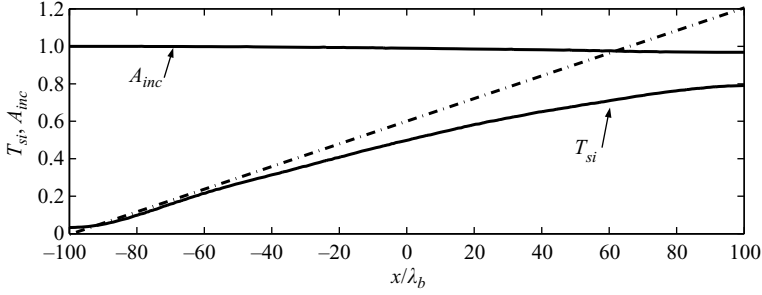


FIGURE 6. Spatial variation of the incident wave amplitude (A_{inc}) and transmission coefficient of the resonant wave (T_{si}) under the exact class II Bragg resonance condition over a bottom patch of sinusoidal ripples. Physical parameters are $h_\ell/h_u = 0.5$, $\mathcal{R} = 0.96$ ($\omega^2 h_u/g = 0.04$), $M_b = 200$, $k_s h_u = 0.16$, $\epsilon_s = 0.005$ and $\epsilon_b = 0.05$ and computational parameters: $N = 2048$, $M = 4$, $T/\Delta t = 64$ and $T_S/T = 120$. Results plotted are the prediction from regular perturbation analysis (Alam *et al.* 2009, (3.22), $-\cdot-\cdot-$) and direct computation ($—$).

condition. Both the numerical simulation result (with $M = 4$) and the theoretical prediction of the regular perturbation and multiple-scale analyses are shown. These results are obtained for $h_\ell/h_u = 0.5$, $\mathcal{R} = 0.96$, $k_s h_u = 0.16$ ($\omega^2 h_u/g = 0.04$), $\epsilon_s = 0.005$, $d/h_\ell = 0.1$, $M_b = 20$, and computational parameters: $N = 2048$, $M = 4$, $T/\Delta t = 64$ and $T_S/T = 80$. The numerical result shows the distinct down shift of the peak amplitude wavenumber $2k_s/k_b$ compared to regular and multiple-scale perturbation predictions, with a magnitude that is found to increase with the bottom steepness. As for the value of the maximum amplitude itself, the HOS result is seen to be somewhat lower than that predicted from regular perturbation and multiple-scale theory. One notes that features of the results for $I_c \xrightarrow{k_b} S_R$ including comparisons of HOS computations and perturbation analyses and higher-order interaction effects are qualitatively similar to the above for $S_c \xrightarrow{k_b} I_R$, and are not repeated.

4.2. Class II Bragg resonance

Alam *et al.* (2009) discussed the condition for class II Bragg resonance involving third-order interactions among one surface (or internal) mode wave and two bottom ripple components given by $\mathcal{D}(k_r, \omega) = 0$ with $k_r = k \pm (k_{b1} \pm k_{b2})$, where k , k_r , k_{b1} and k_{b2} are, respectively, the wavenumbers of the incident wave (of frequency ω), the resonance generated wave and the bottom ripple components. This is a direct extension of class I resonance to the third order, and, as in that case, may similarly involve a resonance generated wave that is transmitted or reflected, and is in the same or different mode as the incident wave.

Figure 6 shows the numerical simulation result for the variation of the transmission coefficients of an incident surface-mode wave and resonance generated internal-mode wave over a patch of bottom ripples under the exact class II Bragg condition. The physical parameters are: $h_\ell/h_u = 0.5$, $\mathcal{R} = 0.96$, $M_b = 200$, $k_s h_u = 0.16$ ($\omega^2 h_u/g = 0.04$), $\epsilon_s = 0.005$ and $\epsilon_b = 0.05$ where the bottom ripple component is counted twice in the class II Bragg resonance interaction. Computational parameters are $N = 2048$, $M = 4$, $T/\Delta t = 64$ and $T_S/T = 120$. For comparison, the regular perturbation prediction of Alam *et al.* (2009) is also plotted. As expected, the numerical and perturbation results agree during the initial growth of the resonance generated wave. As the interaction distance increases, the numerical solution deviates from the linear growth predicted by theory, and eventually decreases after reaching a maximum.

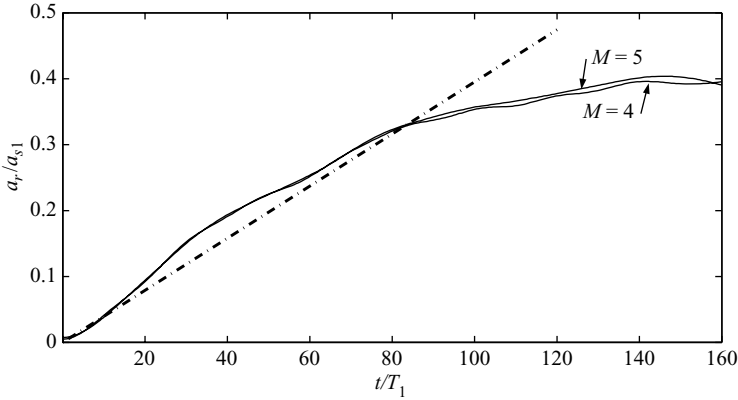


FIGURE 7. Comparison of the regular perturbation result and numerical simulation performed by HOS for resonant internal wave generation under class III Bragg resonance ($S_{c1} + S_{c2} \xrightarrow{k_b} I_R$). Physical parameters are $h_\ell/h_u = 0.42$, $\mathcal{R} = 0.96$, $k_{s1}h_u = 4.3$, $k_{s1}a_{s1} = 0.2$, $k_{s2}/k_{s1} = 0.84$, $k_{s2}a_{s2} = 0.2$, $\epsilon_b = 0.2$ and computational parameters: $N = 2048$, $M = 4, 5$ and $T/\Delta t = 64$.

4.3. Class III Bragg resonance

Class III Bragg resonance occurs when two incident wave components interact with one bottom ripple component to generate a third wave. The major importance of class III Bragg resonance is that, unlike classes I and II, the resonance generated wave has a frequency in general different from those of the incident waves.

For illustration we numerically consider the case of § 5.4 of Alam *et al.* (2009) where two incident surface-mode waves upon interacting with bottom undulations resonate an internal-mode wave ($S_{c1} + S_{c2} \xrightarrow{k_b} I_R$). Numerical simulation is performed in time domain (over a long patch) and with the physical parameters: $h_\ell/h_u = 0.42$, $\mathcal{R} = 0.96$, $k_{s1}h_u = 4.3$ ($\omega^2 h_u/g = 4.3$), $k_{s1}a_{s1} = 0.2$, $k_{s2}/k_{s1} = 0.84$, $k_{s2}a_{s2} = 0.2$ and $\epsilon_b = 0.2$ and computational parameters: $N = 2048$, $M = 4, 5$ and $T/\Delta t = 64$. Figure 7 shows the growth of the amplitude of resonance generated internal-mode wave due to class III Bragg resonance.

In a realistic ocean situation, the above result can be interpreted as follows. In a total water depth of $H = 100$ m with the thermocline at $h_u = 70$ m, two typical ocean surface waves with periods $T_{s1}, T_{s2} = 8.00, 8.75$ s and amplitudes $a_{s1} \sim a_{s2} \sim 3$ m in the presence of bottom ripples of $\lambda_b \sim 160$ m and amplitude $d \sim 5$ m, can resonate a train of relatively high-frequency internal waves ($T \sim 2$ min) with amplitude up to $a_r \sim 1.5$ m. The generated interfacial wave moves in the opposite direction of incident waves and hence scatters back the forward travelling energy of the incident waves.

Features of higher-nonlinearity effects are qualitatively similar to those of class I. They are studied in detail via a number of illustrative examples in Alam (2008).

4.4. Multiple resonance

In practical applications, the incident wave field and/or the bottom topography contain multiple components and combinations that may satisfy the resonance conditions. As these resonant waves are generated, they themselves may satisfy and engage in multiple resonances with the incident/bottom components. While theoretical considerations such as those in Alam *et al.* (2009) provide valuable guidance and fundamental understanding (and results for comparisons for specific cases such as those considered above), extensions beyond these become very complex and the

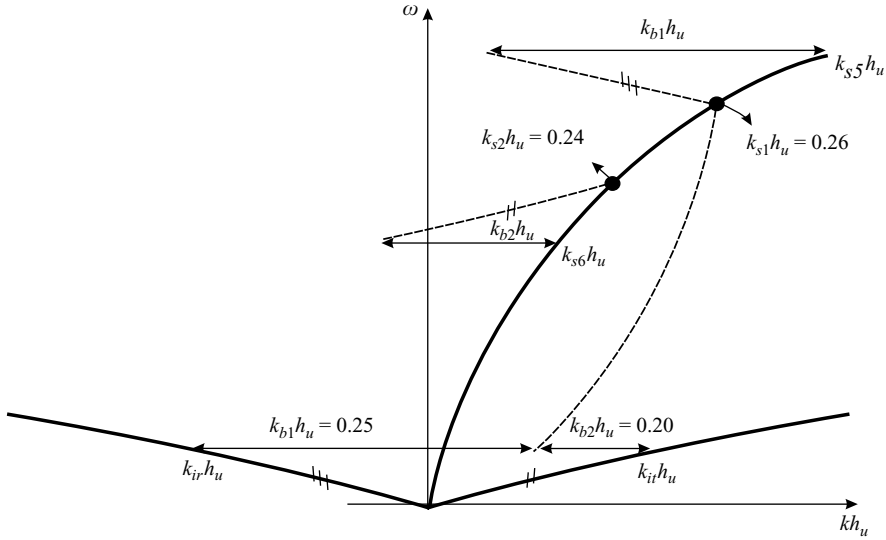


FIGURE 8. Location of multiple resonance points on Ball's diagram.

general problem is intractable. This is one of the main objectives for the development here of the direct numerical simulation capability.

As illustration, we consider a generalized but still relatively simple problem where an incident wave composed of two linearly superimposed wavetrains interacts with a rippled bottom containing two wavenumber components. Our interest is the features associated with the development of multiple resonances and long-time evolutions. For specificity, we choose a configuration with $h_\ell/h_u = 2.3$, $\mathcal{R} = 0.96$ and two surface-mode incident waves with $k_{s1}h_u = 0.26$ ($\omega_{s1}^2 h_u/g = 0.19$), $\epsilon_{s1} = 0.03$ and $k_{s2}h_u = 0.24$ ($\omega_{s1}^2 h_u/g = 0.15$), $\epsilon_{s1} = 0.01$. We consider a bottom ripple patch containing two wavenumber components with dimensionless wavenumbers $k_{b1}h_u = 0.25$ and $k_{b2}h_u = 0.20$ and $k_{b3}h_u = 0.77$ and with the same bottom component amplitudes $d/h_\ell = 0.2$.

For these conditions, it is seen that $k_{s1} - k_{s2} + k_{b2} = k_{i1}$ and $k_{s1} - k_{s2} - k_{b1} = k_{i2}$ (both with the frequency $\omega_i = \omega_{s1} - \omega_{s2}$) satisfy class III Bragg resonance condition with the resonance generated internal-mode wave with wavenumber $k_{i1}h_u = k_{i2}h_u = 0.22$. With these new internal-mode wave and the same bottom components, at the fourth order, two new resonances occur

$$k_{s5} = k_{s1} + k_{i1} + k_{b1} = 0.30/h_u, \quad \omega_{s5} = 2\omega_{s1} - \omega_{s2} \tag{4.1}$$

and

$$k_{s6} = k_{s2} - k_{i1} + k_{b2} = 0.21/h_u, \quad \omega_{s6} = 2\omega_{s2} - \omega_{s1}. \tag{4.2}$$

Note that resonant energy exchange may also occur near the exact resonance points (cf. figures 5). In this case, for instance, the combination of the incident waves k_{s1} and k_{b1} at the third order gives $k_{s1} - 2k_{b1} = -0.24/h_u$ with associated frequency ω_{s1} that does not satisfy the dispersion relation, but is very close to the pair $(-k_{s1}, \omega_{s1})$ which is a resonance point and therefore permits resonant energy exchanges. Figure 8 shows the location of the component of this example on Ball's diagram for the dispersion relationship. In a direct numerical simulation, we use, as initial conditions, the linear

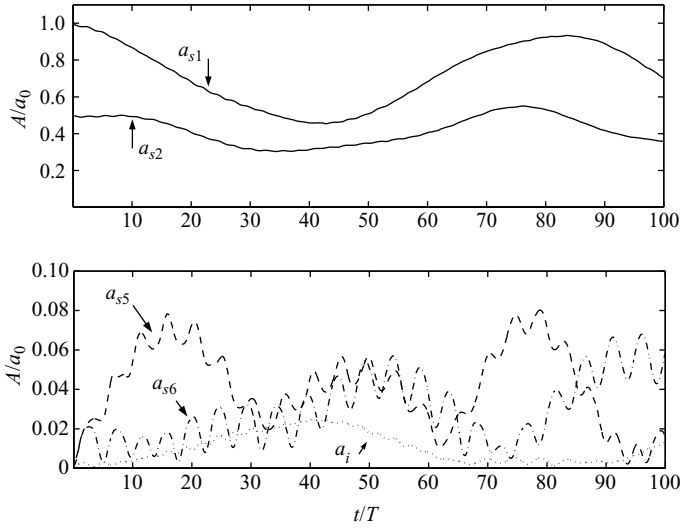


FIGURE 9. Time variation of the amplitudes of the incident waves (—) and resonance generated waves with wavenumbers $k_r = k_{ir} = k_{s1} - k_{s2} - k_{b1}$ and $k_r = k_{it} = k_{s1} - k_{s2} + k_{b2}$ (\cdots); $k_r = k_{s5} = k_{s1} + k_{ir} + k_{b1}$ (- - -); and $k_r = k_{s6} = k_{s2} - k_{it} + k_{b2}$ (- · -).

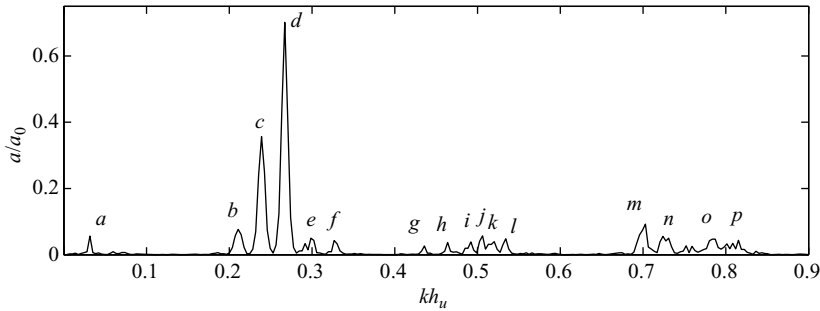


FIGURE 10. Amplitude spectrum of the waves at $t/T = 100$. The letters a – p in the figure indicate wave components with wavenumbers: a , $k_{s1} - k_{s2}$; b , k_{s6} ; c , k_{s2} ; d , k_{s1} ; e , k_{s5} ; f , $3k_{s1} - 2k_{s2}$; g , $k_{s2} + k_{b2}$; h , $k_{s1} + k_{b1}$; i , $k_{s2} + k_{b1}$; j , $k_{s1} + k_{s2}$; k , $k_{s1} + k_{b1}$; l , $2k_{s1}$; m , $3k_{s2}$; n , $2k_{s2} + k_{b1}$; o , $3k_{s1}$; and p , $4k_{s1} - k_{s2}$. All wave amplitudes are measured on the free surface.

solution for the incident surface waves, and computational parameters $N = 1024$, $M = 6$ and dimensionless domain length $L_x = 2\pi$. Figure 9 shows the growth of the amplitudes of the resonance generated waves of k_i , k_{s5} and k_{s6} during the initial stage of the evolution ($t < 100T$). Modulation in time can be observed in the incident and resonance generated waves. A rough correlation can be seen between the minimum of the amplitude of the incident wave and maximum of the amplitude of the resonance generated waves.

Figure 10 plots the spectrum of the nonlinear wave field at $t = 100T$, in which all wave components including both free and locked waves are identified. Note that some of the locked waves are close to the resonant points, and can then be significantly developed in the evolution. Because of this, the wave field becomes increasingly complex as the nonlinear interactions continue. Figure 11(a) shows the time evolution of the amplitude of the first incident surface-mode wave (a_{s1}) and the resonant internal-mode wave (a_i , associated with the class III Bragg resonance). After some

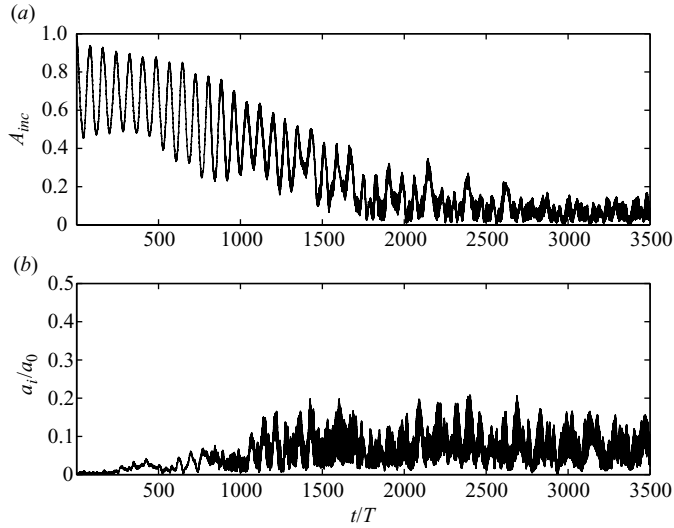


FIGURE 11. Time variation of the amplitudes of (a) the incident wave (a_{s1}/a_0) and (b) the resonant internal-mode wave (a_i/a_0) with wavenumber $k_i h_u = 0.22$.

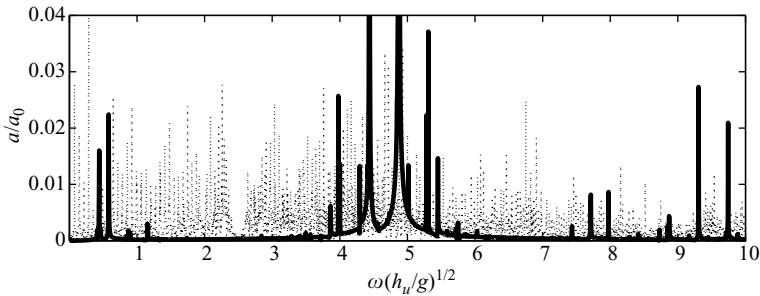


FIGURE 12. Frequency amplitude spectrum of the free surface wave elevation at a fixed location in the wave domain with a flat bottom (—) and a rippled bottom ($\cdot \cdot \cdot$).

regular oscillations during which energy is exchanged between waves (as expected from the perturbation analysis), the variation of the amplitudes of these waves starts to behave irregularly at $t/T \sim 1500$. The loss of order can also be seen in the frequency amplitude spectrum of the free-surface elevation (figure 12), for the free-surface elevation at a fixed point $x=0$ in the time period $2500 < t/T < 3500$. The energy of the wave field, initially confined to two incident free waves (and their higher-order locked-wave harmonics), is now distributed, by multiple resonance and near-resonance interactions with the bottom ripples and among waves, to cover a broadband spectrum. For comparison, and as an independent check, the spectrum of the wave field evolved over the same time with the same initial condition but a flat bottom is obtained also by direct HOS simulation and shown. Figure 13 is the evolution of the amplitude of the incident surface-mode wave (counterpart of figure 11a) when there is no stratification (i.e. $\mathcal{R} = 1$). As can be seen, in the same time frame no (qualitative) loss of order is observed. To quantify the chaotic behaviour of the wave motion, we compute the Lyapunov exponent of this system. We obtain the maximum Lyapunov exponent from the motion history of points on the free surface following classical

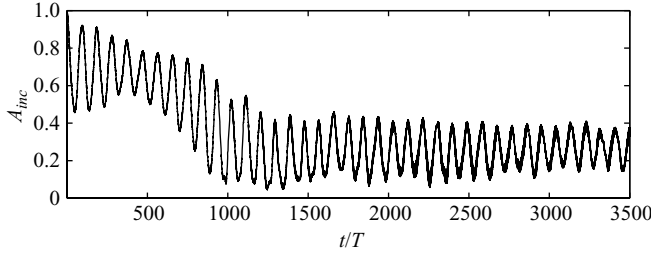


FIGURE 13. Time variation of the amplitudes of the incident wave ($A_{inc} = a_{s1}/a_0$) for the same setup as in figure 11(a) but with $\mathcal{R} = 1$.

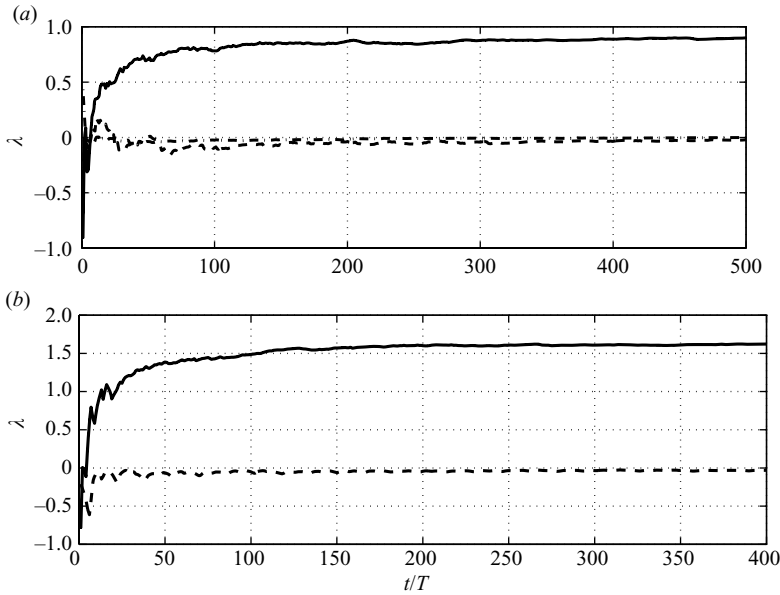


FIGURE 14. Maximum Lyapunov exponent as a function of time for a flat bottom (---) and a rippled bottom (—) for (a) $\mathcal{R} = 0.96$ compared also with no stratification ($\mathcal{R} = 1$, - · -) case and (b) $\mathcal{R} = 0.5$.

methods (e.g. Argyris, Faust & Haase 1994). Figure 14 shows the time evolution of this maximum Lyapunov exponent. The exponent becomes positive after a short initial phase of evolution and approaches an asymptotic (constant) value of $\lambda_{max} \simeq 0.9$ as the evolution continues. In contrast, in the case of uniform depth or no stratification ($\mathcal{R} = 1$), this Lyapunov exponent is non-positive and reaches zero asymptotically.

Initiation of chaos in high-dimensional dynamical systems can be due to a variety of mechanisms (e.g. Temam 1997). The initiation of chaotic behaviour in the present case evidently comes from the mode-coupling of multiple (exact/near) resonances. Figure 15 shows the initial sequence of Bragg resonances and their couplings (using the notation of Alam *et al.* 2009, figures 3 and 4). Also indicated in the figure are the amplitudes associated with the spectrum of figure 10. As these resonances develop and the amplitudes of new resonant waves become appreciable, they participate in yet new interactions of exact and near classes I, II and III (and higher) Bragg resonances as well as (non-Bragg) wave-wave resonances. The final result over increasingly

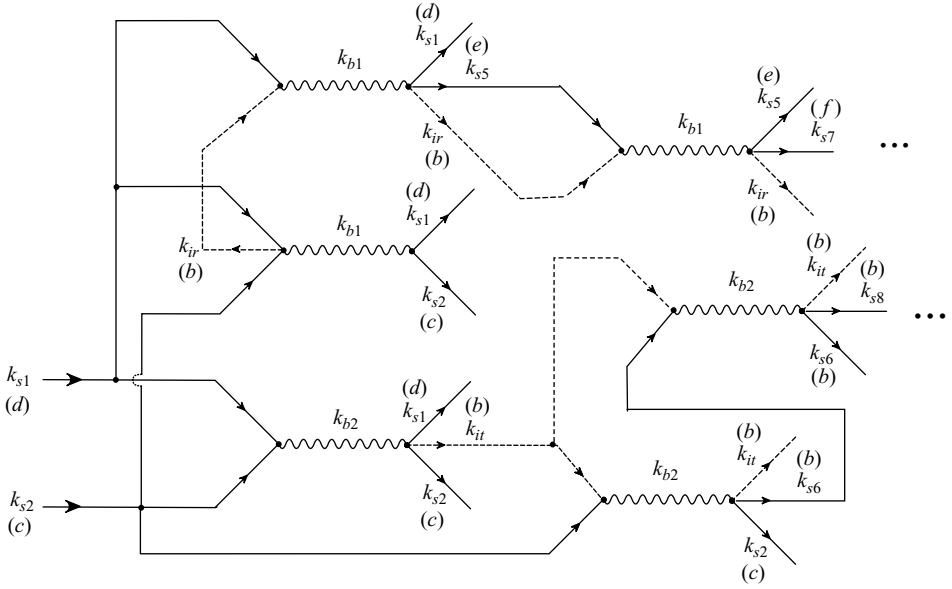


FIGURE 15. Initial sequence of multiple (exact and near) Bragg resonances that eventually lead to chaotic wave motion over long time. The specific Bragg mechanisms for the present case study are indicated using the notation of Alam *et al.* (2009) figures 3 and 4, and the amplitudes of the participating wave modes corresponding to the spectrum in figure 10 are indicated with the letter notation used therein.

greater time scale is the observed irregular wave behaviour with broadband amplitude spectrum.

The observed features of multiple resonances among surface/internal/bottom wave components leading to chaotic wave motion are found to be obtained for broad ranges of physical parameters. In particular, as the stratification strengthens, the time to chaotic motion decreases and the strength of the chaotic behaviour increases. Figure 14(b) shows the maximum Lyapunov exponent for a case with $\mathcal{R}=0.5$ involving initially a single surface-mode incident wave (with $h_\ell/h_u=1$, $k_s h_u=0.30$, $\epsilon_s=0.03$) travelling over a bottom ripple patch containing multiple wavenumber components. The conjugate of this incident wave is an internal-mode wave with wavenumber $k_i h_u=0.73$. Multiple resonances involving different Bragg mechanisms occur for selected sets of bottom component wavenumbers. Figure 14(b) corresponds to a case of a bottom with three wavenumbers given by $k_{b1} h_u=0.36$, $k_{b2} h_u=0.43$ and $k_{b3} h_u=0.77$ and with the same dimensionless amplitude $d/h_u=0.094$.

For these conditions, it is seen that $k_s + k_{b2} = k_i$ satisfies a class I Bragg resonance condition with the resonance generated internal-mode wave with wavenumber $k_i h_u=0.73$ (see figure 16). With this new internal-mode wave and the other two bottom components, two class III Bragg resonances occur $k_{s3} = k_s + k_i - k_{b1} = 0.67/h_u$ ($\omega_{s3} = 2\omega$) and $k_{i3} = k_s + k_i + k_{b3} = 1.8/h_u$ ($\omega_{i3} = 2\omega$) where subscripts $s3, i3$ refer to third-order resonant surface-mode and internal-mode waves. At the fourth order, the interaction among the incident wave k_s , the generated internal wave k_i and two ripple components (k_{b1} and k_{b2}) is nearly resonant and generates an internal-mode wave component with wavenumber $k_{i4} = k_s + k_i + k_{b1} + k_{b2} = 1.82/h_u$ ($\omega_{i4} = 2\omega$).

Figure 17 shows the time evolution of the amplitude of the incident surface-mode wave and the transmitted resonant internal-mode wave in this example. Here the

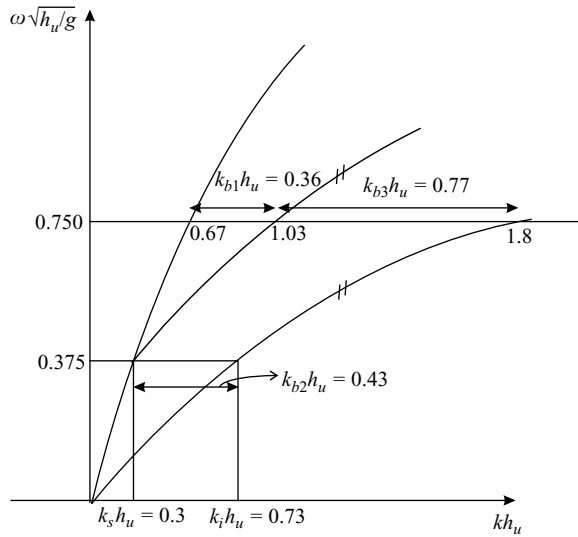


FIGURE 16. Location of multiple resonance points on Ball's diagram.

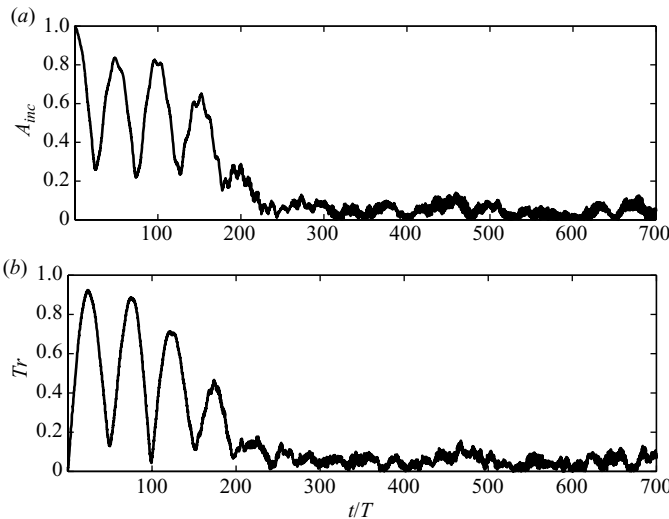


FIGURE 17. Time variation of the amplitudes of (a) the incident wave (A_{inc}) and (b) the transmitted class I resonant internal-mode wave (T_r) with wavenumber $k_i h_u = 0.73$ and frequency $\omega^2 h_u / g = 0.14$.

variation of the amplitudes of these waves starts to behave irregularly at a much shorter time of $t/T \sim 200$ (cf. figure 11a). Figure 14(b) shows that the steady-state value of the maximum Lyapunov exponent is higher than that for $\mathcal{R} = 0.96$ case which is an indication of higher strength chaotic behaviour.

5. Conclusion

To complement the perturbation analyses of Alam *et al.* (2009), an efficient and accurate computational method is developed for the study of general nonlinear

interactions of surface/interfacial waves with variable bottom topography in a two-layer density stratified fluid. The method is based on the extension, to include interfacial waves, of a powerful HOS method originally developed for the study of nonlinear gravity wave-wave and wave-bottom interactions in a homogeneous fluid. The method we developed accounts for nonlinear interactions of surface/interfacial waves with bottom ripples up to an arbitrary high-order M and, as with the original HOS, achieves an exponential convergence with respect to the number of spectral modes N used (for the surface, interfacial and bottom), and an almost linear computational effort with respect to N and M . Systematic validation and convergence tests are performed including the direct comparison to the exact solution of a fully nonlinear two-layer Stokes wave.

The numerical method is used to study a number of canonical problems corresponding to different classes of Bragg resonances and the results are compared to the perturbation results of Alam *et al.* (2009) for these cases. The comparisons are excellent within the region of validity of the perturbation results, deviating typically for longer interaction distance and greater wave/bottom steepness, highlighting the importance of (even) higher order nonlinear interactions not accounted for in the theory.

As a final example, we consider more general but still relatively simple cases involving a single or two incident wave(s) propagating over a rippled bottom containing three/two wavenumber components. By selecting these wavenumbers, conditions for multiple resonances obtained with the resulting evolution leading to the creation of many new Bragg transmitted/reflected waves and eventually chaotic motion after some time.

Although the formulation of our numerical scheme presented here is for two dimensions, the extension to three dimensions in the HOS context is relatively straightforward. This extension has been obtained, for example, for the direct simulation of Bragg resonance in a homogeneous fluid (Liu & Yue 1998) and for the interaction of ambient and Kelvin ship wave (Zhu, Liu & Yue 2008). Oblique class I Bragg resonance is known to be less important than the normal incidence in both a homogeneous fluid (Liu & Yue 1998) and in a two-layer density stratified fluid (Alam 2008). However, this is not necessarily the case for classes II and III Bragg resonance. As in the case of internal wave resonant interactions without bottom effects (e.g. Hill & Foda 1998) and Bragg resonance for a one-layer fluid (Liu & Yue 1998), higher order three dimensional (oblique) Bragg resonance in two-layer stratified fluid may be important and worth further attention.

This research is supported financially by grants from the Office of Naval Research.

Appendix A. Stokes wave for a two-layer fluid using Newton's iterative method

Newton's iterative method can be used to solve the system of nonlinear equations (2.1a)–(2.1h) for the nonlinear permanent wave form (Stokes wave) in a two-layer fluid over a flat horizontal bottom. For convenience, we rewrite (2.1a)–(2.1h) to refer to a coordinate system moving at the phase speed c of the wave and assume a steady solution in this moving frame:

$$\nabla^2 \phi_u = 0 \quad -h_u + \eta_\ell < z < \eta_u \quad (\text{A } 1a)$$

$$\nabla^2 \phi_\ell = 0 \quad -h_u - h_\ell + \eta_b < z < -h_u + \eta_\ell \quad (\text{A } 1b)$$

$$f_1 \equiv -c\eta_{u,x} + \eta_{u,x}\phi_{u,x} - \phi_{u,z} = 0 \quad z = \eta_u \quad (\text{A } 1c)$$

$$f_2 \equiv -c\phi_{u,x} + \frac{1}{2}(\phi_{u,x}^2 + \phi_{u,z}^2) + g\eta_u = 0 \quad z = \eta_u \quad (\text{A } 1d)$$

$$f_3 \equiv -c\eta_{\ell,x} + \eta_{\ell,x}\phi_{u,x} - \phi_{u,z} = 0 \quad z = -h_u + \eta_\ell \quad (\text{A } 1e)$$

$$f_4 \equiv -c\eta_{\ell,x} + \eta_{\ell,x}\phi_{\ell,x} - \phi_{\ell,z} = 0 \quad z = -h_u + \eta_\ell \quad (\text{A } 1f)$$

$$f_5 \equiv \rho_u \left[-c\phi_{u,x} + \frac{1}{2}(\phi_{u,x}^2 + \phi_{u,z}^2) + g\eta_\ell \right]$$

$$-\rho_\ell \left[-c\phi_{\ell,x} + \frac{1}{2}(\phi_{\ell,x}^2 + \phi_{\ell,z}^2) + g\eta_\ell \right] = 0 \quad z = -h_u + \eta_\ell \quad (\text{A } 1g)$$

$$f_6 \equiv \phi_{\ell,z} = 0 \quad z = -h_u - h_\ell. \quad (\text{A } 1h)$$

The solution can be written in the general form which satisfies the respective Laplace equations and the bottom boundary condition:

$$\eta_u(x, t) = \sum_{n=1}^N \eta_{un} e^{ik_n x} + \text{c.c.}, \quad \eta_\ell(x, t) = \sum_{n=1}^N \eta_{\ell n} e^{ik_n x} + \text{c.c.}, \quad (\text{A } 2a)$$

$$\phi_u(x, z, t) = \sum_{n=1}^N \left[\phi_{un}^c \frac{\cosh k_n(z - h_u)}{\cosh(k_n h_u)} + \phi_{un}^s \frac{\sinh k_n(z - h_u)}{\cosh k_n h_u} \right] e^{ik_n x} + \text{c.c.}, \quad (\text{A } 2b)$$

$$\phi_\ell(x, z, t) = \sum_{n=1}^N \phi_{\ell n} \frac{\cosh k_n(z + h_u + h_\ell)}{\cosh k_n h_\ell} e^{ik_n x} + \text{c.c.}, \quad (\text{A } 2c)$$

where N is the number of Fourier modes. The unknown modal amplitudes, η_{un} , $\eta_{\ell n}$, ϕ_{un}^c , ϕ_{un}^s and $\phi_{\ell n}$, $n = 1, \dots, N$, and the unknown phase speed of the wave c are to be determined from the five boundary conditions on the free surface and interface.

To do that, we rewrite these boundary conditions in a symbolic form:

$$\mathbf{F}(\mathbf{X}) = 0, \quad (\text{A } 3)$$

where $\mathbf{F} \equiv \{f_1, f_2, f_3, f_4, f_5\}$ and the unknown vector \mathbf{X} is

$$\mathbf{X} = \{\eta_{u1}, \dots, \eta_{uN-1}, c, \eta_{\ell 1}, \dots, \eta_{\ell N}, \phi_{u1}^c, \dots, \phi_{uN}^c, \phi_{u1}^s, \dots, \phi_{uN}^s, \phi_{\ell 1}, \dots, \phi_{\ell N}\}. \quad (\text{A } 4)$$

Finally, to complete the system, we set $\eta_{uN} = 0$. Newton's iterative method is applied to solve the system of nonlinear equations (A 3) for the unknown vector \mathbf{X} . For an initial guess, the linearized solution is used.

Appendix B. Resonance of waves in a two-layer fluid on uniform depth

Triad resonances in a two-layer density stratified fluid over a flat bottom are known to happen between two surface-mode waves and an internal-mode wave (Ball 1964), and between two internal-mode waves and one surface-mode wave (Wen 1995; Hill & Foda 1996). Here existing theoretical results are invoked to further validate our numerical technique.

Let (a_1, k_1, ω_1) and (a_2, k_2, ω_2) represent the wave amplitudes, wavenumbers and frequencies of the two incident surface waves. The wavenumber and frequency of each wave satisfies the dispersion relation (Alam *et al.* in press (2.7)):

$$\mathcal{D}(k, \omega) = \omega^4 (\mathcal{R} + \coth kh_u \coth kh_\ell) - \omega^2 gk (\coth kh_u + \coth kh_\ell) + g^2 k^2 (1 - \mathcal{R}). \quad (\text{B } 1)$$

If these two incident waves satisfy the resonance condition, i.e. $\mathcal{D}(k_r, \omega_r) = 0$ with $k_r = k_1 + k_2$ and $\omega_r = \omega_1 + \omega_2$, a free internal-mode wave with wavenumber k_r and frequency ω_r will be resonated. The amplitude of the resonant wave initially grows linearly with time. This initial growth can be predicted using regular perturbation

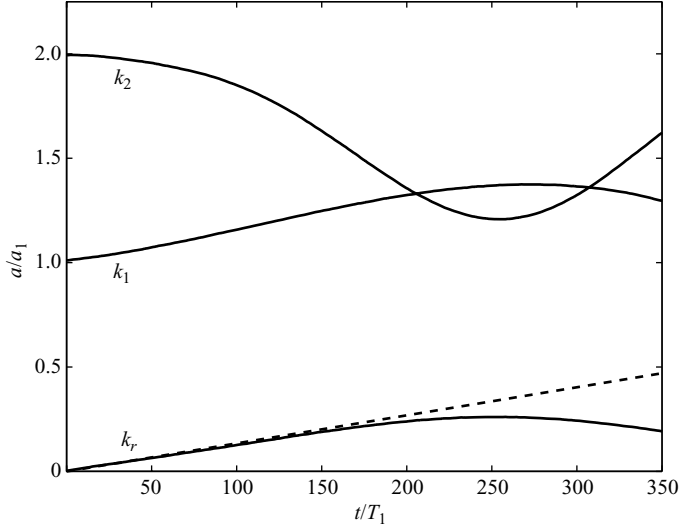


FIGURE 18. Time evolution of the amplitudes of two incident surface-mode waves (wavenumber k_1, k_2) and the resonance generated internal-mode wave (wavenumber k_r) undergoing resonant triad interaction obtained using the present numerical method (—). Plotted for comparison is the regular perturbation prediction for the initial growth of the resonant wave amplitude ((B2), - - -). Chosen parameters are $\mathcal{R} = 0.5$, $h_\ell/h_u = 0.5$, $k_1 h_u = 0.060$ ($\omega_1^2 h_u/g = 0.005$), $a_1/h_u = 0.005$, $a_2/a_1 = 2$, $k_2/k_1 = 2.2$ ($\omega_2^2 h_u/g = 0.025$) and simulation parameters are $L_x = 2\pi$, $N = 512$, $M = 4$ and $T_1/\Delta t = 128$.

analysis to the second order and is given by

$$|\eta_\ell^{(2)}| = \gamma t + \text{non-growing terms}, \quad (\text{B2})$$

where η_ℓ represents the interfacial wave elevation. Expression for the growth rate γ is algebraically complicated and for finite depth is given by, for example, Jamali (1998) and Alam (2008).

Figure 18 shows the variation of the amplitudes of the two (incident) surface-mode waves and the generated internal-mode wave as a function of dimensionless time t/T_1 under the triad resonance condition. The regular perturbation solution gives a growth rate of $\gamma/(a_1/T_1) = 1.3 \times 10^{-3}$ for the generated wave where T_1 is the period of the k_1 wavenumber wave.

For the second resonance, in figure 19, we plot the variation of the amplitudes of the two incident internal-mode waves and the generated surface-mode wave as a function of time. For this example the growth rate of the generated surface-mode wave predicted by regular perturbation analysis is $\gamma/(a_1/T_1) = 2.8 \times 10^{-3}$, which is shown in the figure for comparison. As expected, the present numerical computation and the regular perturbation analysis match well at the initial stage of the interaction, but again deviate at large time as the regular perturbation solution fails.

As a further validation, we compare our numerical results with experiments of Joyce (1974). In set E1 of the experiments, two standing surface-mode waves are set up in a long tank which subsequently generate an internal-mode resonant third wave. Figure 20 compares Joyce (1974) experimental and approximate theoretical results to the present HOS simulation. The initial growth agrees well with the experiment and approximate theoretical results. However, the curves deviate as time grows. In the experiment, the surface waves are continuously forced by a paddle, hence the

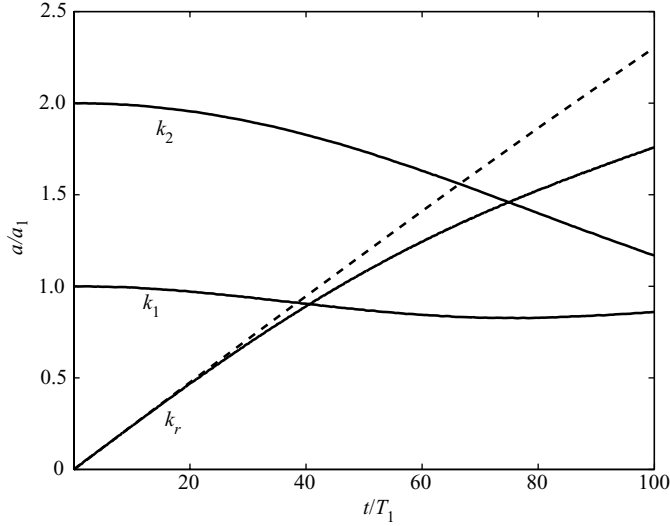


FIGURE 19. Time evolution of the amplitudes of two incident internal-mode waves (wavenumber k_1 , k_2) and the resonance generated surface-mode wave (wavenumber k_r) undergoing resonant triad interaction obtained using the present numerical method (—). Plotted for comparison is the regular perturbation prediction for the initial growth of the resonant wave amplitude (derived similarly to (B2), - - -). Chosen parameters are $\mathcal{R} = 0.5$, $h_\ell/h_u = 0.5$, $k_1 h_u = 0.13$ ($\omega_1^2 h_u/g = 7 \times 10^{-4}$), $a_1/h_u = 0.005$, $a_2/a_1 = 2$, $k_2/k_1 = 0.45$ ($\omega_2^2 h_u/g = 3 \times 10^{-3}$) and for numerical simulation $L_x = 2\pi$, $N = 512$, $M = 4$ and $T_1/\Delta t = 512$.

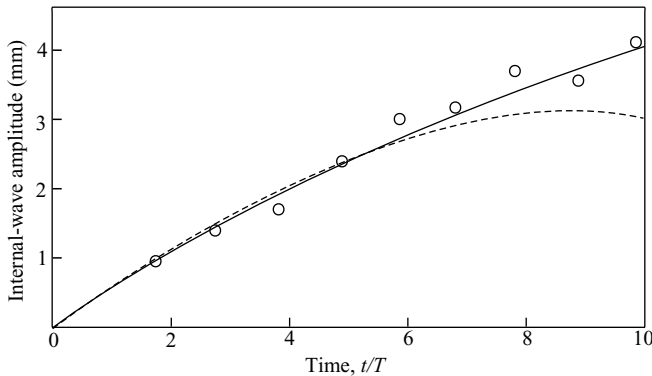


FIGURE 20. Time evolution of the amplitudes of the resonant (standing) internal-mode wave corresponds to the experiment E1 of Joyce (1974) with two standing surface-mode waves of $\omega_1 = 18.20 \text{ rad s}^{-1}$ and $\omega_2 = 17.72 \text{ rad s}^{-1}$ in a 2 m long tank with $\mathcal{R} = 1.000/1.049 = 0.953$ and $h_\ell/h_u = 0.6/0.3 = 2.0$ and with initial amplitude of $a_1 = 3.77 \text{ mm}$ and $a_2 = 2.68 \text{ mm}$. An internal-mode wave of frequency $\omega_r = 0.484 \text{ rad s}^{-1}$ will satisfy a triad resonance condition, hence its amplitude will grow with time (shown in this figure). For the simulation the total length of the tank is assumed to be 18 m and $NDX = 1024$, $M = 4$ and $T/\Delta t = 1024$. Plotted are theoretical (—) and experimental (○) results of Joyce (1974) and numerical simulation with HOS (- - -). The discrepancy at large times comes from the assumption of constant surface wave amplitude in Joyce (1974) work.

amplitude of the two forcing surface waves remain constant. In the HOS simulation, we start with the same initial condition as of the experiment, but do not add external energy to the domain. Therefore, as expected, the forcing and resonant wave amplitudes exhibit modulation in time as energy goes back and forth among them.

Appendix C. Determination of reflection and transmission coefficients

Our objective is to obtain the numerical predictions of quantities such as the spatially varying reflection and transmission coefficients and compare these to existing theoretical results. The HOS simulation captures the nonlinear interactions among all the surface/interfacial wave and bottom ripple components (up to the specified order M) as they evolve in time. The HOS wave field (in space and time) thus contains wave components that include surface and internal-mode free and locked waves associated with the incident and the resonance generated waves, including those that have the same frequencies but different wavenumbers, etc. It should also be pointed out that because of nonlinearity in the simulations, these components in general do not satisfy (exactly) linear dispersion relationships. We describe here a robust scheme to extract the quantities of interest from such wave fields.

Our approach is an extension/improvement of the method of Goda & Suzuki (1976), which we find to be not sufficiently robust for the present application. Without loss of generality, assume a wave field containing two surface wave components with the same frequency ω but different wavenumbers k_1 and k_2 given by

$$\eta(x, t) = a_1(x) \cos(k_1 x - \omega t + \psi_1) + a_2(x) \cos(k_2 x - \omega t + \psi_2), \quad (\text{C } 1)$$

where a_1 , a_2 and ψ_1 , ψ_2 are respectively the (slowly varying) amplitudes and phases of the two waves. Given $\eta(x, t)$ in the computational domain over a certain period of time, the objective is to determine $a_1(x)$ and $a_2(x)$ for (C 1). To capture the slowly varying $a_1(x)$ and $a_2(x)$, we first represented them by Chebyshev polynomials

$$a_1(x) = \sum_{n=1}^{N_T} \alpha_{1n} T_{n-1}(x), \quad a_2(x) = \sum_{n=1}^{N_T} \alpha_{2n} T_{n-1}(x), \quad (\text{C } 2)$$

where T_n is the n th order Chebyshev polynomial of the first kind, α_{1n} and α_{2n} the unknown modal amplitudes and N_T the number of Chebyshev modes retained in the expansion. The unknown coefficients α_{1n} and α_{2n} can be obtained from known values of $a_1(x_j)$ and $a_2(x_j)$ at collocation points x_j for the Chebyshev polynomial.

To find $a_1(x_j)$ and $a_2(x_j)$ at some collocation point x_j , we choose a small window W_j centred at $x = x_j$ with a length of $\Delta \ell$ generally much smaller than the length of the entire wave field. Inside this window, we again represent $a_1(x)$ and $a_2(x)$ in expansions of the form of (C 2) using N_{Tj} terms where N_{Tj} can be somewhat smaller than N_T . For the present work, we find that typical values of $N_T = 6$ or 7 , and $N_{Tj} = 2$ or 3 adequate to obtain accurate (smooth) predictions of the transmission/reflection coefficients. We now define $q = 1, \dots, L_j$ uniformly spaced points in W_j and write

$$\eta(x_q, t) = \eta_j^c(x_q) \cos(\omega t) + \eta_j^s(x_q) \sin(\omega t), \quad q = 1, \dots, L_j, \quad x_q \in W_j. \quad (\text{C } 3)$$

At each x_q within W_j , the amplitudes $\eta^c(x_q)$ and $\eta^s(x_q)$ are obtained using Fourier transform in time of the wave field time histories at that point. Note that $\eta_j^c(x)$ and $\eta_j^s(x)$ contain fast dependence on x . Substituting the expansions for the amplitudes in W_j into (C 1) and equating the result with (C 3), we obtain for each x_q two equations for the unknown modal amplitudes at that point. For the window W_j , we have together a system of $2L_j$ linear equations for $2N_{Tj}$ unknown Chebyshev coefficients and two phases for that window. This system is typically over-determined with $L_j \gg N_{Tj}$, and the unknown amplitudes (and phases) are obtained using least squares. With these modal amplitudes determined, we obtain $a_1(x_j)$ and $a_2(x_j)$ at the centre of W_j .

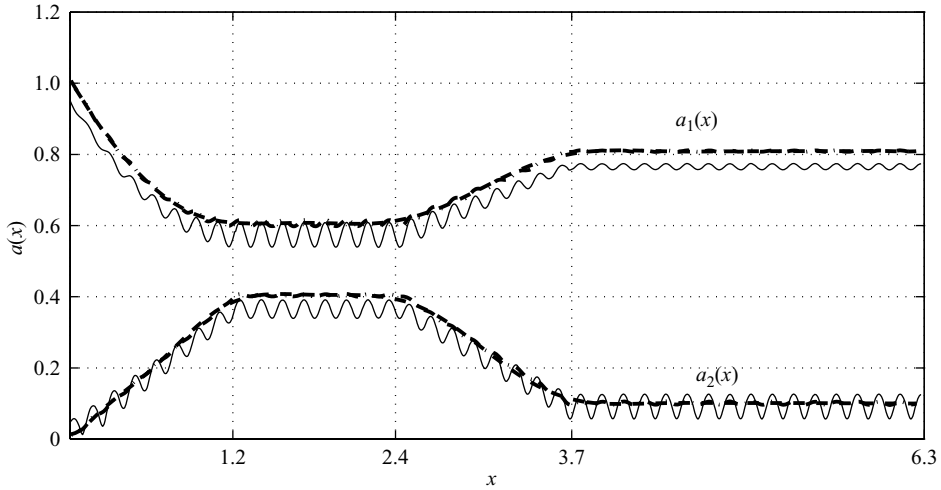


FIGURE 21. Spatial variations of the slowly varying amplitudes of a two-component wavetrain obtained using the present scheme (— · —) and the method of Goda & Suzuki (1976) (—), compared with the exact solution (· · ·). Note that the solution using the present scheme is graphically indistinguishable from the exact solution.

We repeat this process for a large number of collocation points (relative to N_T) for $a_1(x_j)$ and $a_2(x_j)$ from which the expansion coefficients α_{1n} and α_{2n} in (C 2) can be obtained, say, by using the orthogonality of Chebyshev polynomials. We remark that the scheme of Goda & Suzuki (1976) corresponds to the local (W_j) step only (without (C 2)) of the present scheme with the simplest choice of $N_{Tj} = 1$ and $L_j = 2$.

As an illustration, we consider a sample synthetic wave field given by the superposition of two wave components with wavenumbers $k_1, k_2 = 32, 72$, and slowly varying amplitudes $a_1(x)$ and $a_2(x)$ given by the ‘exact’ curves in figure 21. Since in practice the wavenumbers are not exactly known/given, to show the robustness of the scheme, we do not use the exact but instead approximate values of the wavenumbers $\tilde{k}_1, \tilde{k}_2 = 30, 76$ in the assumed decomposition (C 1). Figure 21 shows the predicted amplitudes $a_1(x), a_2(x)$ obtained using the present algorithm and those using the method of Goda & Suzuki (1976) as compared to the exact functions. In this case, the Goda & Suzuki (1976) predictions show highly oscillatory behaviour with mean values deviating somewhat from the exact curve. In contrast, the predictions using the present scheme are graphically indistinguishable from the exact result.

Appendix D. Simulation over long patches

The case of wave evolution over a very long bottom patch of (periodic) ripples is discussed analytically in Alam *et al.* (2009), §B.2. Figure 22 shows numerical simulation of such a case for an incident surface-mode wave, where the time variations of amplitudes of the incident (surface mode) and resonance generated (internal mode) waves obtained by numerical simulations, and comparison to those from perturbation analyses. The physical parameters are $h_\ell/h_u = 0.5$, $\mathcal{R} = 0.96$, $k_s h_u = 0.16$ ($\omega^2 h_u/g = 0.04$), $\epsilon_b = 0.1$ and for two incident wave steepnesses $\epsilon_s = 0.0005$ and 0.0050 . Note that although the initial surface steepness is small, since the transmission coefficient is greater than unity, the steepness of resonant internal reaches high values ($\epsilon_i > 0.2$) where the effect of nonlinearity becomes important. The results in figure 22

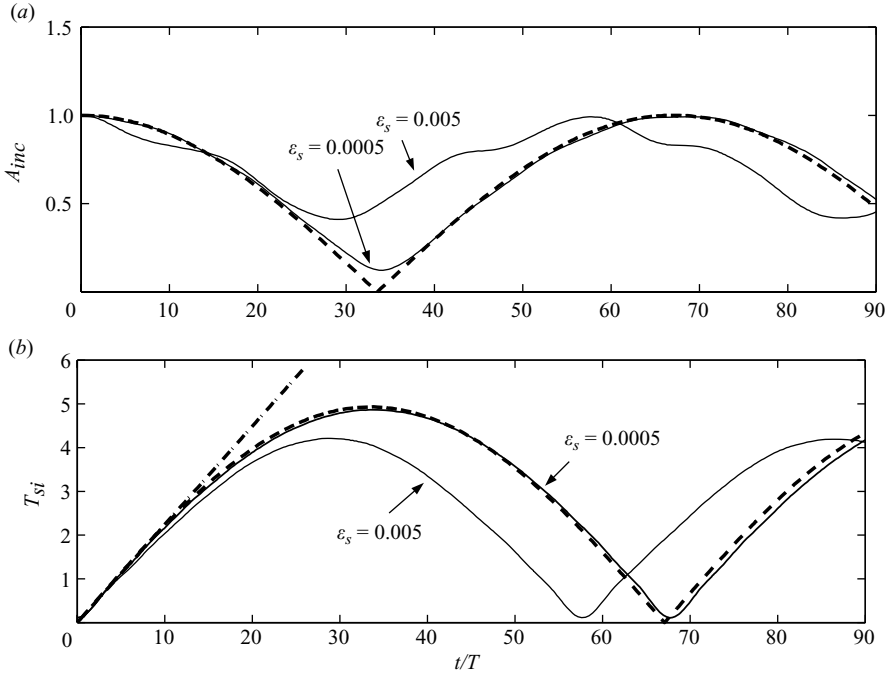


FIGURE 22. Temporal variation of (a) the amplitude of the incident surface-mode wave (A_{inc}) and (b) the transmission coefficient of resonance generated internal-mode wave (T_{si}) over a periodic patch of bottom ripples under class I Bragg resonance condition. Physical parameters are $h_l/h_u = 0.5$, $\mathcal{R} = 0.96$, $k_s h_u = 0.16$ ($\omega^2 h_u/g = 0.04$), $\epsilon_b = 0.1$ and computational parameters: $N = 2048$, $M = 4$, $T/\Delta t = 64$. Results plotted are: numerical simulation (—) for $\epsilon_s = 0.0005$ and 0.0050 and predictions from regular perturbation (derived from Alam *et al.* 2009, (3.16), $-\cdot-$) and multiple-scale analyses (Alam *et al.* 2009, (B9), $- - -$).

display similar features to those for the spatial variations of the amplitudes over a finite patch of bottom ripples. The regular perturbation solution, which predicts a linear growth with time for the resonant wave and a constant amplitude for the incident wave, compares well with the multiple-scale analysis and the nonlinear HOS computation in the initial evolution for $t/T < 10$. Beyond the initial development, the regular perturbation solution of the resonant wave amplitude diverges as t increases while the multiple-scale analysis and HOS computation show periodic oscillatory time variations for the amplitudes of both incident and resonant waves. For relatively mild incident waves, the prediction of the multiple-scale analysis matches perfectly to the HOS computation. As the incident wave steepness increases, the HOS result deviates from the (leading-order) multiple-scale analysis prediction with decreases in both the amplitude and period of the time modulations. This effect of higher-order nonlinear interactions on the evolution appears consistent with all the other cases we considered.

REFERENCES

- ALAM, M.-R. 2008 Interaction of waves in a two-layer density stratified fluid. PhD thesis, Massachusetts Institute of Technology, Cambridge, MA.
- ALAM, M.-R., LIU, Y. & YUE, D. K. P. 2009 Bragg resonance of waves in a two-layer fluid propagating over bottom ripples. Part I. Perturbation analysis. *J. Fluid Mech.* **624**, 225–253.

- ARDHUIN, F. & MAGNE, R. 2007 Scattering of surface gravity waves by bottom topography with a current. *J. Fluid Mech.* **576**, 235–264.
- ARGYRIS, J., FAUST, G. & HAASE, M. 1994 *An Exploration of Chaos*. North-Holland Publishing Co.
- ATHANASSOULIS, G. A. & BELIBASSAKIS, K. A. 1999 A consistent coupled-mode theory for the propagation of small-amplitude water waves over variable bathymetry regions. *J. Fluid Mech.* **389**, 275–301.
- BALL, F. 1964 Energy transfer between external and internal gravity waves. *J. Fluid Mech.* **19**, 465–478.
- BOEGMAN, L., IMBERGER, J., IVEY, G. N. & ANTENUCCI, J. P. 2003 High-frequency internal waves in large stratified lakes. *Limnol. Oceanogr.* **48** (2), 895–919.
- CUMMINS, P. F., VAGLE, S., ARMI, L. & FARMER, D. M. 2003 Stratified flow over topography: upstream influence and generation of nonlinear internal waves. *R. Soc. Lond. Proc. Ser. A Math. Phys. Engng Sci.* **459** (2034), 1467–1487.
- DOMMERMUTH, D. G. & YUE, D. K. P. 1987 A higher-order spectral method for the study of nonlinear gravity waves. *J. Fluid Mech.* **184**, 267–288.
- DOMMERMUTH, D. G. & YUE, D. K. P. 1988 The nonlinear three-dimensional waves generated by a moving surface disturbance. In *Proceedings of 17th Symposium on Naval Hydrodynamics*, Hague, Netherlands, pp. 918, 923. National Academy Press.
- GODA, Y. & SUZUKI, Y. 1976 Estimation of incident and reflected waves in random wave experiments. In *Proceedings of 15th Coastal Engng Conference*, Honolulu, Hawaii. Pp. 828–845.
- HILL, D. F. & FODA, M. A. 1996 Subharmonic resonance of short internal standing waves by progressive surface waves. *J. Fluid Mech.* **321**, 217–233.
- HILL, D. F. & FODA, M. A. 1998 Subharmonic resonance of oblique interfacial waves by a progressive surface wave. *R. Soc. Lond. Proc. Ser. A Math. Phys. Engng Sci.* **454** (1972), 1129–1144.
- JAMALI, M. 1998 Surface wave interaction with oblique internal waves. PhD thesis, The University of British Columbia, Vancouver, Canada.
- JOYCE, T. M. 1974 Nonlinear interactions among standing surface and internal gravity waves. *J. Fluid Mech.* **63** (04), 801–825.
- LIU, Y. & YUE, D. K. P. 1998 On generalized Bragg scattering of surface waves by bottom ripples. *J. Fluid Mech.* **356**, 297–326.
- MIROPOL'SKY, Y. Z. 2001 *Dynamics of Internal Gravity Waves in the Ocean*, *Atmospheric and Oceanographic Sciences Library*, vol. 24. Kluwer Academic Publishers.
- TEMAM, R. 1997 *Applied Mathematical Sciences*, vol. 68: *Infinite-Dimensional Dynamical Systems in Mechanics and Physics*, 2nd edn. Springer-Verlag.
- WEN, F. 1995 Resonant generation of internal waves on the soft sea bed by a surface water wave. *Phys. Fluids* **7** (8), 1915–1922.
- ZAKHAROV, V. E. 1968 Stability of periodic waves of finite amplitude on the surface of deep fluid. *J. Appl. Mech. Tech. Phys.* **2**, 190–194.
- ZHU, Q., LIU, Y. & YUE, D. K. P. 2008 Resonant interactions between Kelvin ship waves and ambient waves. *J. Fluid Mech.* **597**, 171–197.